Hydrous Shear Zones in the Lower Arc Crust are sites of Melt Transfer

Aditi Chatterjee

Department of Earth and Environmental Sciences

Faculty of Science and Engineering
Macquarie University, Sydney, NSW 2109

June 29, 2022

A thesis submitted in partial fulfillment of the requirements for the degree of Master of Research

DECLARATION

I declare that this thesis, as a whole or in parts, has not been submitted for a higher degree to any other university or institution. To the best of my knowledge and belief, the thesis contains no material previously published or written by another person except where due reference is made in the thesis itself.

I wish to acknowledge the following assistance with the research detailed in this thesis:

Funding for this project was provided by Australian Research Council Discovery Project funding. Nathan Daczko and Stephen Foley supervised this research project. Legacy geochemistry data was compiled from the literature, and legacy samples collected by Helen Degeling (University of Sydney, Hons, 1997) and GNS Science, New Zealand, were used in this project. The thin sections were prepared by Thin Section Australia, Queensland. Robyn Gardner digitized the thin sections, Sean Murray did the BSE imaging of whole thin sections, and Kim Jessop collected the zircon BSE images. Joyjit Dey and Sandra Piazolo ran the EBSD maps at the University of Leeds, UK, and provided the software training. The thesis was reviewed and edited by Nathan Daczko, Robyn Gardner, Kim Jessop, Joyjit Dey, and Sandra Piazolo. All other research was done by the candidate.

No ethics approval was required for this project.

29th June 2022

Aditi Chatterjee

This thesis is prepared and formatted in the style of a manuscript for submission to the *Journal of Metamorphic Geology,* with some exceptions to meet the requirements of the Macquarie University. This includes the requirement of an abstract of 200 words, 2 cm margins, 1.5x line spacing, figures, and tables embedded within the text.

TABLE OF CONTENTS

ACKNOWLEDGEMENTS

Completing a Master of Research thesis during a pandemic was challenging. Therefore, I am very thankful to everyone who has supported me this past year. First and foremost, I would like to thank Assoc. Prof. Nathan Daczko and Prof. Sandra Piazolo, for devoting their time and energy towards helping me complete this project. Nathan, thank you for assisting me through every step of the thesis with your extensive knowledge of microstructures, Fiordland, and metamorphic geology. Sandra, thank you for facilitating the EBSD analysis of my samples for this project and teaching me how to frame an argument and present it. I thank my co-supervisor, Prof. Stephen Foley, for inviting me to his group meetings and providing feedback and encouragement during my MRes journey. Further, thanks to Dr. Ajay Narendra for his helpful advice and quick response throughout this time.

I would also like to thank Dr. Robyn Gardner for her reviews and advice at almost every step of my project. I thank Dr. Kim Jessop for her feedback and comments on my thesis. Moreover, I would like to thank Dr. Hindol Ghatak for all his support from the beginning, from helping me understand the enrolment process to providing feedback for my figures and writing. Also, a big thanks to GRA for providing an extension and helping me with all the administrative queries.

A heartfelt thanks to Rida, Muhammad, Mustaqeem, Taufeeq, and Babar for being my second family in the UK. Thanks for caring for us when we had COVID. Thanks, Babar, for making us laugh with all your fun stories. Rida, thanks for inviting me to your place almost every other day for dinner. Taufeeq, thanks for the fantastic breakfast. Going on long drives with Mustaqeem made our days less gloomy. Last but not least, thank you, Muhammad, for playing peek-a-boo with me (hopefully, you will be able to read this yourself in a few years when you start learning the alphabet).

Then, I would like to thank my family. Firstly, a warm thanks to my parents, Ashish and Archita, and my brother Anirban for their support through all the ups and downs. Thanks to my husband Joyjit for being a pillar of support in this journey. Many thanks to my in-laws, Rituparna, Arati, and Uttam, for their constant encouragement. Thanks to Prof. Joydip Mukhopadhyay for his help and support. Last but certainly not least, a big thanks to Prof. Abhijit Bhattacharya for sharing his wealth of knowledge and for always being there for me.

Candidate's statement about the impact of COVID-19 changes on the thesis

Dear Examiner,

Many of our HDR candidates have had to make changes to their research due to the impact of COVID-19. Below you will find a statement from the candidate, approved by their Supervisory Panel, that indicates how their original research plan has been affected by COVID-19 restrictions. Relevant ongoing restrictions in place caused by COVID-19 will also be detailed by the candidate.

Candidate's Statement

The initial research plan for my Master of Research thesis was significantly altered due to the closed Australian borders. Although I planned to move to Australia in September 2021, I spent the entire MRes research year without coming to Macquarie University due to extended border closures and the difficulty of international travel. I worked remotely from India and the UK. My work plan needed to be re-adjusted multiple times. The thesis was going to be more heavily based on high pressure-temperature experiments in the Foley Laboratory at Macquarie University. Instead, this thesis focused on the microstructural and geochemical aspects of a lower crustal shear zone in Fiordland, New Zealand.

Moreover, due to COVID restrictions, fieldwork or access to the laboratory equipment for petrographic and geochemical analysis was not possible. In the end, I worked using legacy samples from the University of Sydney and GNS Science, New Zealand, and legacy geochemical data. In 2021 and 2022, we collaborated with Prof. Sandra Piazolo at the University of Leeds, UK, for analysis. However, research at the University of Leeds was also affected by the COVID lockdown. Hence, there was a delay in collecting the analytical data needed for research. Additional EBSD re-analysis of some samples and laboratory analyses, e.g., additional whole rock geochemistry and electron microprobe mineral chemistry, were planned. However, lockdown-related delays pushed these analyses out of the timeframe for this thesis. I was COVID positive and ill for three weeks, and I am highly thankful to the Graduate Research Academy for extending my thesis submission deadline by three weeks.

ABSTRACT

Recent studies of the lower arc crust exposed in Fiordland, New Zealand, concluded that shear zones are sites of melt migration and mass transfer through the deep crust. The 4-10 km-wide George Sound Shear Zone (GSSZ) in central Fiordland comprises two main rock types, relatively dry two-pyroxene gneisses, and hornblende-bearing gneisses.

Petrographic analysis of samples collected in a transect across the shear zone shows a range of hydration reaction textures from rims of hornblende + quartz around pyroxene grains to complete replacement of pyroxene grains. Plagioclase is recrystallized and partially replaced by clinozoisite. Additionally, biotite mode increases from outside the shear zone towards higher strain rocks. BSE images and polarised light microscopy show microstructures indicative of former melt-present deformation: (a) interconnected mineral films of K-feldspar along grain boundaries, (b) grains that terminate with low dihedral angles, (c) interstitial grains, (d) undulose extinction in plagioclase and (e) serrated grain boundaries.

From the above observations, it is inferred that a felsic to intermediate hydrous melt migrated along the GSSZ through two-pyroxene gneiss host rocks. The melt migration along grain boundaries was deformation-assisted, which hydrated pyroxene to hornblende + quartz, plagioclase to clinozoisite, and introduced high proportions of biotite into the assemblage.

Chapter 1: INTRODUCTION

Subduction of oceanic crust at convergent plate boundaries drives partial melting of the mantle wedge above the subducting plate. This tectonic setting is the Earth's most active and involves heat and mass transfer, forming a vast array of igneous rocks and ultimately driving the chemical evolution of the Earth's crust. Subduction zones are essential sites of continental growth, geochemical cycling, tectonic-climate coupling, ore formation, geothermal energy production, earthquakes, volcanism, and other natural hazards (e.g., Zheng, 2019).

Melt migration is a crucial process within a subduction tectonic setting that transfers arc magma from its mantle wedge source through the wedge and crust to the surface. The ascent of magma is primarily driven by pressure gradients where the melt is drawn towards sites of lower pressure and ultimately moves towards the surface (Robin, 1979; Sawyer, 1994). At high proportions of melt (>10%), the fluid overpressure and differential buoyancy of connected melt pockets within the surrounding rocks facilitates the ascent of melt (Spence et al., 1987). The more common situation of lower melt fraction requires deformation to enhance the rock permeability and create pressure gradients to promote melt migration (Maaløe, 1982; Meek et al., 2019, Hasalova et al., 2008).

Deformation-assisted melt migration involves deformation-induced dilatancy that forms pressure gradients during crystal plastic creep processes such that melt is drawn toward sites of active deformation (Etheridge et al., 2021). The most understood deformation-assisted melt migration mechanisms are dyking in the brittle regime and flow through zones of high strain deformation (i.e., shear zones) in the ductile regime, as they can be observed in the rock record at an outcrop scale. However, the currently recognized number and volume of these channeled melt pathways are not enough to accommodate the mass and heat transfer needed for the chemical differentiation of the crust (Rudnick, 1995). This discrepancy could be addressed by the lesser-explored third mode of melt transfer of diffuse porous melt flow in the crust (Brown, 2010; Hasalova et al., 2008; Sawyer, 1999; Weinberg, 1999).

Despite its importance, melt transfer and pathways through the Earth's crust are not well understood, especially in the middle and lower crust. Recent research over the past five years in the Pembroke Valley, Fiordland, New Zealand (Figure 1 inset, marked PV), has identified

meter to tens-of-meter scale deformation-assisted diffuse melt transfer zones through magmatic lower arc crust (Daczko et al., 2016; Stuart et al., 2018; Meek et al., 2019). Zones of high strain in the Pembroke Granulite acted as an important melt migration pathway and are identified as an open system (Stuart et al., 2018; Meek et al., 2019). Evidence recorded by hydration, metasomatism, and rare earth element mobility, bolstered by the preservation of abundant microstructures indicative of the former presence of melt, suggests diffuse melt flow through the high-strain rocks (Stuart et al., 2016; Stuart et al., 2018; Meek et al., 2019) of the Pembroke Valley (Figure 1 inset). However, the prevalence of deformation-assisted melt transfer through high-strain zones in other regions in the Fiordland (Figure 1 inset) lower arc crust is yet to be thoroughly explored.

The Pembroke Valley is a small part of a large area of exposed lower arc crust of a Cretaceous magmatic arc in Fiordland, New Zealand (Mortimer et al., 1999; Tulloch & Kimbrough, 2003; Figure 1). Fiordland's remaining area of the lower crust is dominated by one plutonic suite, the Western Fiordland Orthogneiss (Figure 1; Allibone et al., 2009). Mapping of this unit shows multiple plutons of similar composition that are variably recrystallized to eclogite, granulite, and amphibolite facies assemblages. The Worsley and Misty plutons in the north (Figure 1) comprise two-pyroxene diorite, monzodiorite, and monzonite in the center, surrounded mainly by hornblende diorite that may or may not contain relict pyroxene. Rare igneous two-pyroxene assemblages are preserved, but widespread recrystallization at granulite facies formed the predominant rock type, a two-pyroxene gneiss (Bradshaw, 1989; Bradshaw 1990; Allibone et al., 2009).

Peripheral components of the Worsley and Misty plutons and much of the McKerr Intrusives (Figure 1) are rich in hornblende and biotite. Some of these rocks are inferred to have crystallized from a more hydrous magma than the central part of the plutons, as dykes of hornblende diorite are observed to cut the two-pyroxene gneisses (Allibone et al., 2009). However, relict corroded pyroxene and symplectite intergrowths of hornblende-quartz occur widely in the peripheral components of the plutons. This demonstrates that some of the hornblende-rich rocks are hydrated versions of the two-pyroxene rocks (Allibone et al., 2009), similar to textures formed during melt-rock interaction in deformation-assisted melt transfer zones in the Pembroke Valley to the north (Daczko et al., 2016; Stuart et al., 2018; Meek et al., 2019). This similarity in microstructures highlights the possibility of an open system melt

migration as a potential driver of the hydration reaction textures in the peripheral components of the Worsley and Misty plutons.

The early penetrative gneissosity in the two-pyroxene components of the northern plutons is cut by the middle to lower crustal, kilometer-scale, NNE-trending George Sound Shear Zone (dashed lines in Figure 1, Klepeis et al., 2004). This shear zone coincides with the hornblende-rich eastern margin of the Misty Pluton and cuts through the hornblende-rich eastern McKerr Intrusives (Figure 1). Additionally, the shear zone fabrics in the Worsley Pluton in the north are defined by both two-pyroxene and hornblende-rich assemblages (Allibone et al., 2009). However, whether the protolith to these deformed hornblende gneisses is a two-pyroxene gneiss or a hornblende diorite is still unclear. The potential role of melt migration through the George Sound Shear Zone (GSSZ) leading to the metamorphic overprinting of the pyroxene gneiss to form hornblende gneiss is yet to be examined. Further, the current study can contribute to our knowledge of the importance of deformation-assisted diffuse melt transfer through high-strain zones in the lower crust of magmatic arcs.

Based on the above observations and interpretation, there are two competing hypotheses for the formation of the hornblende-rich domains of the Western Fiordland Orthogneiss (WFO). The first is the classic interpretation, hypothesis 1: hornblende-rich rocks crystallized from a water-rich component of the Western Fiordland Orthogneiss magmatic system, which are subsequently variably deformed (Allibone et al., 2009). An alternative view, which is the focus of this current work, is hypothesis 2: hornblende-rich rocks formed during melt-rock interaction that hydrated a two-pyroxene-rich protolith as hydrous melt migrated through the crust via the high strain zone (i.e., George Sound Shear Zone).

In order to investigate these competing hypotheses, this research compares and contrasts the existing viewpoints using (i) geochemical data available in the literature and (ii) a microstructural investigation of selected rock thin sections. This project aims to test the second hypothesis that the Western Fiordland Orthogneiss comprised of two-pyroxene gneisses were overprinted by metamorphic processes and underwent hydration reactions to form hornblende gneiss during melt-rock interaction. In this model, the George Sound Shear Zone acted as a conduit for a reactive melt to percolate through the Western Fiordland Orthogneiss. This led to the formation of the hydrous hornblende gneisses. Studying the evolution of the hornblende gneiss around the George Sound Shear Zone will not only help us understand melt

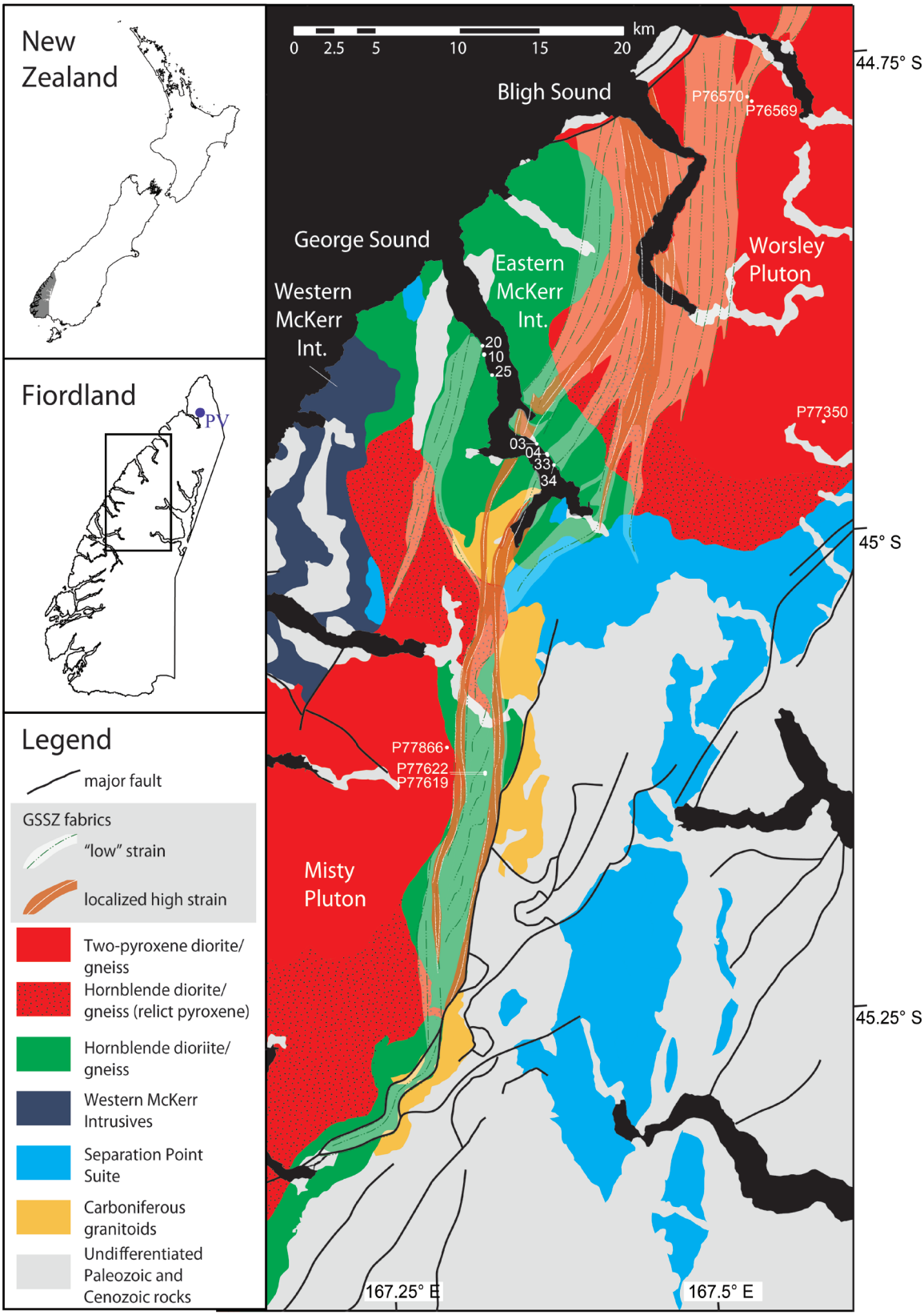

Figure 1: *Map of Fiordland, New Zealand, showing: (i) two main Cretaceous mid-lower crustal plutonic suites, the Western Fiordland Orthogneiss (WFO, shown in* ***red****,* ***green****, and dark gray) and Separation Point Suite (****blue****), and (ii) the extent of George Sound Shear Zone (GSSZ). Pyroxene gneiss and Hornblende gneiss components of the Western Fiordland Orthogneiss are distinguished by color and stippled pattern (see legend). (iii) PV (****purple****) on the inset is the Pembroke Valley. Modified after Lindquist (2020). NOTE: last two digits of 97 samples are marked.*

migration through the lower arc crust but also contribute to our knowledge regarding mass and heat transfer in the crust.

1.1 Background Knowledge:

1.1.1 *Melt transfer and high strain zones*

Melting begins in pelitic and felsic rocks as the temperature rises above 650°C (Sawyer, 1999). Mafic rocks melt at a higher temperature depending upon their bulk composition, volatile content, and confining pressure (Breton & Thompson, 1998; Sawyer, 1999). Minerals in the rock begin to melt as the temperature crosses the respective solidus for a given bulk rock composition. Initially, the melting starts at triple point junctions of grains and forms isolated melt pockets. With the rising heat, the melt volume increases, and the melt pockets become interconnected (Sawyer, 1999). According to Maaløe (1982) and Sawyer (1999), the system requires 5% melt or more for the pockets to connect. However, the threshold value for the rock to become permeable depends upon the bulk rock composition and deformation (Maaløe, 1982; Sawyer, 1999).

The degree to which the melt is connected affects the rock's rheology and active mechanisms during deformation (Rosenberg & Handy, 2005). The presence of melt in the rock leads to a significant decrease in rheology, weakening the rock and generating a high strain zone, which further acts as a pathway for the melt to percolate (Holyoke & Tullis, 2006; van der Molen & Paterson, 1979). A decrease in the rock strength can be observed as the melt-free rock transitions to rock with an interconnected melt network (Rosenberg & Handy, 2005). This phenomenon is termed the melt-connectivity threshold (MCT). There are two broad types of deformation behavior within the melt-connectivity threshold depending upon the melt fraction, (i) low melt fractions (1-4%) (Dell' Angelo & Tullis, 1988; Walte, Bons, & Passchier, 2005), and (ii) moderate melt fractions (<8%) (Walte et al., 2005). At low melt fractions, the deformation is characterized by grain boundary migration (GBM) and dislocation creep, and it is characterized by lobate or serrated boundaries, subgrains, and undulose extinction. At moderate fractions, grain boundary sliding (GBS) takes over, where the grains slide past each other while drawing the melt towards the high strain zone. In this case, the melt is present around the grain boundaries, forming a rheologically weak layer that accommodates the deformation, leaving no traces of internal deformation in the minerals. On the other hand, when

the melt percentage is greater than 20 to 25%, the entire solid framework breaks down and limits grain boundary migration (Vanderhaeghe, 2009). So, depending upon the melt content, the melt transfer pathways change.

Apart from the melt fraction, two additional factors determine the style of melt migration: the driving force and the site to which the melt is migrating (Sawyer, 1999). Melt segregation is primarily driven by active deformation (Sawyer 2001), which leads to the further ascent of magma. There are two commonly discussed modes of melt transfer: dykes in the brittle regime (Sleep, 1988; Spence et al., 1987; Weinberg, 1996) or flow through shear zones in the ductile regime (Beach & Fyfe, 1972; Carter & Dwarkin, 1990; Cartwright & Barnicoat, 2003). Recent works have shown that a third mechanism is possible: diffuse porous melt flow in the lower crust, but it is yet to be explored extensively (Stuart et al., 2016; Meek et al., 2019).

In previous work examining the lower crust in arc settings, three styles of porous diffuse melt flow have been identified in the rocks of the Pembroke Granulite (Daczko et al., 2016; Stuart et al., 2018; Meek et al., 2019): Style I partial melt assisted diffuse porous melt flow that partially hydrates a two- pyroxene gabbroic protolith; Style II rectilinear dyking and formation of adjacent garnet reaction zones; and Style III syndeformational melt transfer in and near shear zones. Deformation leads to melt localization and enhances diffuse melt-flux through the high strain zones. Significant time-integrated diffuse grain boundary melt-flux can allow considerable volumes of melt to migrate over time via high strain zones in the crust.

High-strain zones acting as a conduit for a high volume of melt (>10%) can be easily recognized from pockets, seams, and dykes of leucosomes in the outcrop (Brown & Solar, 1998; Colin & Sawyer, 1996). In contrast, recognizing high strain zones associated with low to moderate volumes of melt (1-8% melt) is challenging. The melt pockets and interstitial grains formed by low to moderate melt volume are too small and dispersed to be identifiable in the outcrop scale, so a microscopic study is necessary (Dell' Angelo & Tullis, 1988; Walte, Bons, & Passchier, 2005). A recent study (Stuart et al., 2018) has identified some of the key microstructures of the former presence of melt in high strain zones with lower melt fractions.

The microstructures indicative of the former presence of melt are discussed in section 1.1.2 below.

1.1.2 *Microstructures indicative of the former presence of melt*

Identifying the microstructures indicative of the former presence of melt is important as it provides insights into the melt transfer processes and potential melt-rock interactions. Some outcrops may clearly indicate the presence of former melt in the form of dykes or sills. However, some rocks, especially those with lower melt percentages, do not demonstrate the former presence of melt at the outcrop scale but require microscale investigation.

A list of textures documented by Sawyer (1999) & Vernon (2011) provides criteria for the recognition of the former presence of felsic melt in a static system, which includes: 1) an aggregate of three minerals, quartz, K–feldspar, and sodic plagioclase in veins, 2) euhedral grains of feldspar or felsic protoleucosomes lined by peritectic minerals, 3) feldspar grains with simple twinning, 4) minerals subtending to low dihedral angles ($<60^{o}$) between two other grains (i.e., a felsic mineral between two mafic minerals), 5) overgrowths of euhedral feldspar without inclusions, 6) cuspate grains of quartz, K-feldspar or sodic plagioclase, 7) veinlets of plagioclase with higher Na content than the adjacent plagioclase grains in the rock, 8) biotite pseudomorphed by feldspar, 9) plagioclase with oscillatory zoning, 10) microgranophyric intergrowths of alkali feldspar and quartz in patches or veins, 11) symplectic aggregates of minerals, and 12) melanosome patches and layers. The set of microstructures observed in a rock can vary depending upon factors like the bulk composition of the rock, the melt composition, and the melt migration processes.

This project investigates hypothesis 2 mentioned before in the introduction, i.e., melt transfer through an actively deforming high strain zone that reacts with the surrounding pyroxene-gneiss to form hornblende gneiss. Therefore, the list of microstructural indicators from Sawyer (1999) & Vernon (2011) is narrowed down to five key textures to identify the former presence of melt in high strain zones. Further, this is also discussed in the recent work of Stuart et al. (2018) in the Pembroke Valley (Figure 1 inset). The five key microstructures are as follows: 1) low dihedral angles of interstitial phases, 2) elongate interstitial grains or films, 3) small aggregates of quartz grains in association with xenomorphic plagioclase grains, 4) fine-grained K-feldspar bearing multiphase aggregates that may or may not be surrounded by augite grains, and 5) millimeter- to centimeter-scale felsic dykelets. However, all the five textures mentioned may or may not be found in melt transfer events through high strain zones, depending on the melt vs. precursor rock compositions, style of deformation, and melt transfer mechanisms.

Combining the knowledge from previous literature, the criteria for recognizing former melt in high strain zones employed in this project are expanded here. They are as follows:

(i) Low (≤ 60°) dihedral angle of interstitial grains

The minerals with low dihedral angles trace areas of former melt that may have been connected (depending upon its viscosity) during the melt migration along grain boundaries. Grains that subtend a low dihedral angle of 60° or less at the junction of three mineral grains are inferred to pseudomorph melt (Holness, 2006; Vernon, 2011). The low dihedral angle may appear at the terminal end of elongate grains (see 1.1.2(ii) next) or continue into films along the grain boundary. In contrast, most minerals develop dihedral angles greater than 60° in melt-free metamorphic processes (Beere, 1975; Hasalova et al., 2008; Holness, 2006; Holness and Sawyer, 2008; Rosenberg and Riller, 2000; Stuart et al., 2018b; Vernon, 2011). Recent works have observed quartz and K-feldspar grains displaying low dihedral angles in plagioclase-rich rocks and inferred the former presence of melt (Holness & Sawyer, 2008; Levine et al., 2013; Stuart et al., 2018; Vernon, 2011).

(ii) Elongate interstitial grains and boundary films

Elongate interstitial grains are thin, high aspect ratio minerals observed between two other mineral grains. These elongate grains with thin, tapered ends commonly display low dihedral angles. Melting experiments conducted by Laporte (1994) produced melt films along grain boundaries. These small-scale micro-structures are commonly inferred to have pseudomorphed former melt (Sawyer, 2001; Stuart et al., 2016; Stuart et al., 2018).

(iii) Cuspate grain boundary

Grains that partly penetrate along the grain boundary between two other minerals form a concave outward boundary, also described as a cuspate grain boundary (Harte et al., 1991; Holness and Sawyer, 2008; Marchildon and Brown, 2002; Rosenberg and Riller, 2000; Sawyer, 1999; Sawyer, 2001; Vernon, 2011). Studies have identified mineral grains with cuspate grain boundaries and subtending a low dihedral angle in rocks that were once exposed to melt-rock interaction, and it is inferred that grains with cuspate boundaries could indicate the former presence of melt (Harte et al., 1991; Holness & Sawyer, 2008; Marchildon & Brown, 2002;

Rosenberg & Riller, 2000; Sawyer, 1999; Sawyer, 2001; Vernon, 2011). However, cuspate boundaries can also be observed in a solid-state metamorphic rock where one grain hinders the growth of the other (Holness & Clemens, 1999; Vernon, 2011). Hence, cuspate grains should be paired with other indicators of former melt when used as evidence to determine the former presence of melt.

(iv) Symplectites

Symplectites are intergrowths of two or more minerals that replace another mineral. These fine-grained intergrowth textures may partially or wholly pseudomorph the original mineral (Vernon, 2011; Winter, 2014). Melt-rock reaction is one key process that can lead to the formation of symplectites. Hence, they can act as an additional indicator for the former presence of melt. As symplectites also form in response to changes in pressure, temperature, and/or the introduction of other fluids such as water (Vernon, 2011; Winter, 2014), they should also be used in conjunction with other evidence of the former presence of melt.

(v) Zircon grains

Unlike many other minerals, zircon is highly resistant and can survive during magmatic and metamorphic processes. The grains of zircon record these episodes in the form of varied textures such as core and rim zonation (Corfu et al., 2003). These textures cannot be studied using a petrographic microscope. Instead, it requires high-resolution techniques like back-scattered electron (BSE) or cathodoluminescence (CL) imaging. Apart from U-Pb dating, the microstructures preserved in a zircon grain may also record the events occurring during its evolution (Halpin et al., 2020; Corfu et al., 2003). Annealing and lattice reorganization above 600° C can occur in a zircon grain, leading to Pb loss (Mezger & Krogstad, 1997). Breakdown of any modally abundant phase with tens of parts per million (ppm) Zr can contribute to the formation of zircon grains (Mezger & Krogstad, 1997; Morriset & Scoates, 2008). For example, zircon rims can be observed around ilmenite grains (Morriset & Scoates, 2008). The zircon rims can form from the diffusion of Zr from ilmenite to grain boundaries during reaction with available Si (Morriset & Scoates, 2008).

Precipitation of zircon grains is possible in the presence of an intergranular melt that carried or resorbed Zr from the other phases (Roberts & Fingers, 1997; Varvra et al.,1999). The growth

of newly precipitated zircon grains and rims may have crystal facets, mainly when growing against a free melt phase (Pidgeon et al., 1998, Schaltgegger et al., 1999, Vavra et al., 1999, Halpin et al., 2020). Secondary processes that modify zircon include the replacement of zircon by a secondary zircon in the presence of a metamorphic fluid (Halpin et al., 2020). The reaction front progresses from the grain boundary to the core of the primitive zircon (Pidgeon et al., 1998, Schaltgegger et al., 1999, Vavra et al., 1999). Such processes are termed coupled dissolution-precipitation, which leaves textural marks in the zircon grains, such as the preservation of a reaction front and porosity that may be distributed patchily through the grain or form trails transecting the grains (Halpin et al., 2020). The nucleation and growth of new faceted zircon grains, crystallization of overgrowths forming new zircon rims, or the modification of existing zircon via coupled dissolution-precipitation are likely indicators of the former presence of melt.

Along with microstructural evidence, melt-rock interaction can lead to significant changes in the geochemistry of the rock, which is discussed in section 1.1.3 below.

1.1.3 *Chemical changes during melt-rock interaction*

Melt migration through the crust can be considered an open thermodynamic system. Since the melt has a composition different from the surrounding rock, it is expected that the melt will react with the surrounding rock. Reactions can enrich or deplete elements in the minerals, leaving behind a chemical footprint. Such chemical signatures help trace the melt transfer process and its consequences.

Even though, theoretically, it is predicted that there is a diffuse porous transfer of melt in the deeper crust, evidence from natural case studies is limited. A recent study of diffuse melt transfer through the lower arc crust, now exposed in the Pembroke Valley, Fiordland (Stuart et al., 2018), records minor modifications of the whole-rock chemical data. When melt migrates through an interconnected channel, the melt reacts with the surrounding rock, forming reaction product minerals along the pathways. These minerals may shield the melt from reacting further with the pathway rocks. Hydration reactions in the pathways necessitate the availability of H_2O, which may come from the melt or the breakdown of other hydrous minerals (Stuart et al., 2018). Melt migration pathways at the grain scale were identified where plagioclase grains are enriched in Sr and Na (Stuart et al., 2018).

According to Stuart et al. (2018), four different styles of melt-rock interactions were identified in the magmatic arc roots exposed in the Pembroke Valley, New Zealand, and these were studied for their geochemical signatures. The four styles are *Style 1*: "Diffuse porous melt flow," *Style 2*: "Channelised porous melt flow," *Style 3*: "Deformation-assisted porous melt flow," and *Style 4*: "Reactive infiltration, followed by melt flux through an armoured zone." Following melt-rock interactions, Styles 1, 2, and 3 produced bulk rock compositions similar to the precursor rocks, excluding the addition of the volatile component. Therefore, these styles of melt migration do not necessarily produce a recognizable geochemical change at the whole rock scale. However, Style 4 is consistent with melt-driven metasomatism, and there are differences in major and rare earth element (REE) composition in the bulk rock compared to the protoliths. Due to the higher temperature and higher time-integrated melt flux in Style 4, the bulk composition significantly changed over time. Homogeneity of mineral compositions was observed in Styles 2, 3, and 4, while Style 1 lacked equilibration and showed variation in mineral compositions and zonation. This equilibration in Styles 2, 3, and 4 are due to the higher time-integrated volumes of melt-flux and a higher degree of modification and recrystallization.

Rare earth elements (REEs) are redistributed between the minerals in Styles 1, 2, and 4, but no sign of enrichment or depletion is observed at the whole rock scale (Stuart et al., 2018). This is interpreted to be facilitated by the presence of an interconnected network of melt that enables the efficient diffusion of rare earth elements. By comparison, Style 3 is associated with heterogeneity in the REE patterns of minerals. Style 3 has a component of active deformation during melt flux which might localize melt flux, limiting the effective volume of rock in contact with the melt and hence hindering the efficient distribution of REEs throughout. The heterogeneity might also be explained by numerous reactivations and multiple episodes of melt-flux through the high strain zone. In addition to REEs, the trace elements might also be enriched or depleted during the melt-transfer events in Style 3: "Deformation-assisted porous melt flow."

Two key factors, i) time-integrated melt flux and ii) spatial distribution of the melt network, impact the geochemical evolution during melt-rock interactions. These parameters are, in turn, controlled by factors such as deformation, temperature, buoyancy, and porosity present in the rocks during the melt flux. Therefore, the geochemical signature preserved in a rock following a melt-rock interaction event can be employed as an indicator for the style of melt transfer and the associated physical parameters. The Western Fiordland Orthogneiss, cross-cut by George

Sound Shear Zone in Fiordland, New Zealand (Figure 1), is a well-preserved part of the lower crustal magmatic arc from the Early Cretaceous. The area forms an excellent natural case study of the interplay between melt-flux and deformation that is studied in this research via the examination of microstructures and geochemical analysis.

1.2 Regional Geology:

The Western Fiordland Orthogneiss dominantly comprises three main plutons: Misty, Worsley, and Malaspina, along with the McKerr Intrusives and several other smaller intrusive bodies. For this project, the northern plutons Misty and Worsley, along with the McKerr Intrusives (Figure 1), are examined within and adjacent to the George Sound Shear Zone (Figure 1). The plutons were emplaced between 114 Ma and 128 Ma (Schwartz et al. 2017).

The McKerr Intrusives are divided into eastern and western units that grade into each other. The eastern McKerr Intrusives (128.3–120.1 Ma) comprise diorite, quartz diorite, and quartz monzodiorite, with xenoliths of granitic and metasedimentary rocks (Bradshaw & Kimbrough, 1991; Allibone et al., 2009). The western McKerr Intrusives (118.4-117.7 Ma) are heterogeneous and composed of diorite, quartz monzodiorite, tonalite, granodiorite, and monzonite (Schwartz et al., 2017; Allibone et al., 2009).

The Worsley Pluton (124-121.8 Ma) is composed of a two-pyroxene diorite, monzodiorite, and monzonite at its core, with hornblende diorite in the outer margins (Schwartz et al., 2017; Allibone et al., 2009). The younger Misty Pluton (116.8-114.2 Ma) comprises three main lithologic units: a two pyroxene ± hornblende diorite and monzodiorite core in the central and western region; a diorite and quartz monzodiorite with relict pyroxene (partially replaced by hornblende) in the south; and hornblende-rich diorite with strong foliation that occurs along the eastern margin within the George Sound Shear Zone (Allibone et al., 2009). The foliated hornblende-rich, diorite-rich domain shares fault contact with Palaeozoic plutons, metasediments, and carboniferous plutons to the east.

Decker et al. (2017) suggested that the plutons crystallized from a magma that was at least partially mantle-derived. Pressure during the emplacement of the Worsley and the Misty pluton is calculated as approximately 0.5-1.1 GPa (Allibone et al., 2009). The plutons were further subjected to pressures greater than 1.2 GPa due to crustal thickening (Allibone et al., 2009;

Bradshaw, 1990). Coupled with pressure and the heat from the emplacement, the Western Fiordland Orthogneiss and its host rocks underwent high-grade metamorphism and deformation (D1) to form a regional gneissocity (S1). Geobarometric data analysis from Worsley and Misty Plutons suggests an emplacement of 35-50 km; for McKerr Intrusives, it is 20-35 km (Anderson et al., 2019).

The George Sound Shear Zone (GSSZ; D2) (dashed line in Figure 1) cross-cuts the Western Fiordland Orthogneiss (WFO). It is defined by an NNE to N striking, steeply-dipping foliation (S2) that forms an amphibolite-grade high-strain zone (Allibone et al., 2009). Marcotte et al. (2005) estimated that the shear zone was active between 119 Ma and 111 Ma. Paired with the belt of Carboniferous plutons, this shear zone is also suggested to be a crustal scale boundary from the isotopic analysis of Klepeis et al. (2019).

East of the Western Fiordland Orthogneiss is the Separation Point Suite (Figure 1), emplaced between 123 Ma – 116 Ma, which is suggested to be the upper to mid crustal equivalent (Allibone et al., 2009) of the lower crustal Western Fiordland Orthogneiss. The Early Cretaceous Separation Point Suite was formed during the final magmatic stage of an extensive arc system. The suite comprises sodium-rich, alkali-calcic diorite to biotite-hornblende monzogranite (Allibone et al., 2009).

Chapter 2: METHODS

This project aims to investigate the two-competing hypotheses, (1) classic igneous origin (Allibone et al., 2009) vs. (2) role of metamorphic overprinting, towards the evolution of the lower crustal arc rocks in and around the George Sound Shear Zone. Hence, this project utilizes published field data, legacy rock samples, and geochemical data in the northern plutons Misty, Worsley, and McKerr Intrusives around the George Sound Shear Zone in Fiordland, New Zealand. The methods revolve around reviewing the existing data and samples with conventional and high-end quantitative techniques like electron backscatter diffraction (EBSD) to assess hypothesis 2.

The lower crust plays a pivotal role in melt transfer to the upper crust and the geochemical evolution of the crust. In Fiordland, Separation Point Suite is accepted as the upper to the mid crustal equivalent of the lower crustal Western Fiordland Orthogneiss (Allibone et al., 2009; section 1.2). So, a set of whole-rock geochemical data was compiled based on extensive published literature for two plutonic suites in Fiordland, New Zealand (Western Fiordland Orthogneiss and Separation Point Suite, Figure 1). The purpose of studying the two plutonic suites was to investigate the geochemical variation across the broader area (section 2.1, below).

Rock samples were only selected from the Western Fiordland Orthogneiss, as the project's key focus is to study the lower crustal arc. The samples were obtained from collections housed at (1) The University of Sydney, from the honours thesis collection of Helen Degeling (Degeling, 1997); and (2) GNS Science, selected using the Petlab database (https://pet.gns.cri.nz/#/), New Zealand's national rock, mineral, and geo-analytical database. Polished thin sections were made for seven rock samples from the Degeling collection and six rock samples from the GNS Science collection (Table 1). Detailed further analysis was conducted on three samples from the Degeling (1997) collection and five from the GNS Science collection, giving a good geographical distribution of analyzed samples along the George Sound Shear Zone (Figure 1). Mineral assemblages, microstructures, and crystal orientation data were studied using polarised light microscopy, scanning electron microscopy (SEM), and electron backscatter diffraction (EBSD) analysis (discussed in sections 2.2, 2.3, and 2.4 below).

2.1 Whole-rock Geochemistry:

Whole-rock geochemical data for 111 rock samples from the Western Fiordland Orthogneiss (WFO) and 204 rock samples from the Separation Point Suite (SPS) were obtained from the published literature and the GNS Science Petlab database (see Supplementary data). The 111 legacy data points from the Western Fiordland Orthogneiss comprise rocks sampled in and around the George Sound Shear Zone region, i.e., from the three northern units of the Western Fiordland Orthogneiss: Worsley Pluton, Misty Pluton, and McKerr Intrusives (Figure 1). All other components of the Western Fiordland Orthogneiss were excluded.

The outliers in the database were studied rigorously by examination of hand samples and by preparing additional thin sections to investigate the mineral assemblages carefully. Most samples from the three northern units were included in the database. However, some were excluded if they met any of the following criteria: (i) samples with unusual mineral assemblages, such as garnet-bearing samples (n=2), (ii) samples located very close to the margins of the plutons and possibly contaminated (n=3), (iii) minor components of the Western Fiordland Orthogneiss such as dykes or inclusions (n=2), and (iv) for one sample where a hand sample or thin section was not available for review.

Detailed fieldwork combined with meticulous observation of microstructures was necessary to classify the pyroxene gneisses according to the degree of hydration. The compiled dataset had 111 samples. However, it was not possible to gather all the 111 thin sections and study them. In this study, pyroxene being the key mineral in the transition of pyroxene gneiss to hornblende gneiss (hypothesis 2), the 111 samples of Western Fiordland Orthogneiss were classified into two broad groups: (1) 'dry' and (2) 'wet,' based on pyroxene mineral modes. The database comprises 61 'dry' rock samples of Western Fiordland Orthogneiss containing pyroxene (i.e., including relict grains of pyroxene) and 50 'wet' rock samples of Western Fiordland Orthogneiss lacking pyroxene and rich in hydrous minerals.

Petrographic inspections were made for an additional twenty thin sections of Western Fiordland Orthogneiss, for which whole rock geochemistry was compiled in order to split the available geochemical database into samples containing pyroxene (i.e., 'dry' rock) and samples containing no pyroxene (i.e., 'wet' rock).

After a detailed investigation of the data set, the geochemical data points of 'dry' and 'wet' rocks from Western Fiordland Orthogneiss and Separation Point Suite were plotted using Microsoft Excel.

Even though the data has been collected from several publications, the general routine followed for the whole-rock XRF data analysis is briefly presented here. Whole-rock geochemical analyses of representative samples are performed by crushing fresh, unaltered samples using a hydraulic press with tungsten carbide plates until rock fragments are < 1 cm^3. Sample fragments are reduced to a fine powder using a tungsten carbide barrel and ring tema mill. Further, the major and trace elements are measured via X-ray Fluorescence (XRF). Compiled geochemical data include major and trace elements from X-ray fluorescence (XRF) analysis, predominantly gathered by Spectrachem Laboratories, Lower Hutt, New Zealand (Allibone et al., 2009).

2.2 Petrographic Analysis:

In order to maintain consistency, the classification of rock samples for petrographic analysis was the same as the geochemical data set discussed in section 2.1. Rock samples from the Western Fiordland Orthogneiss for the thin section study were also broadly classified into two groups based on petrographic analysis of pyroxene mineral modes (1) 'dry' - contains pyroxene and (2) 'wet' – no pyroxene (Table 1). Samples classed as 'dry' are pyroxene-bearing gneisses with low proportions of hydrous minerals (total mode of hydrous minerals < 25%). Some 'dry' samples contain relict grains of orthopyroxene or clinopyroxene partially replaced by amphibole-rich symplectites. In contrast, 'wet' samples are hornblende gneisses that lack pyroxene (i.e., pyroxene mode = 0%). The 'wet' rocks are rich in hydrous minerals, including hornblende, biotite, and clinozoisite (total mode of hydrous mineral > 25%). The mineral modal percentages are calculated using ImageJ software (Table 2).

Thin sections (30 μm) were prepared at Thin Section Australia, in Brisbane, Queensland, and at GNS Science, New Zealand, from blocks cut from representative samples. The blocks were cut following the XZ plane of the kinematic frame of reference with 'X' parallel to lineation and 'Z' perpendicular to the foliation. Mineral identification and microstructural relationships of the samples were determined using plane-polarized light and cross-polarized light microscopy, along with high-resolution backscattered electron images of whole thin sections (see sections

2.3, 2.4). Due to the COVID lockdown and limited access to the microscope, digitized images of the thin sections were studied online via ImageMatrix.

The thin sections are available at the link https://imagematrix.science.mq.edu.au/gallery/ and searching for the keyword 'WFO.' The mineral abbreviations mentioned in this project were taken from Whitney & Evans (2010).

2.3 Backscattered electron (BSE) Imaging:

Backscattered electron images were used to identify the minerals and microstructures at a higher resolution. Polished thin sections of the samples were carbon coated and imaged using an FEI Teneo Field Emission Scanning Electron Microscope (SEM) with Nanomin software at Macquarie Geo-Analytical, Macquarie University. The operating conditions of the SEM were a high vacuum, at an accelerating voltage of 10 kV, and a dwell time of 2 μs. Stitched images of whole thin sections were created and uploaded to ImageMatrix as layers for each sample. They were further used for identifying different phases and their distribution in the studied samples. Further analyzed in detail for textures, grain size, and crystal preferred orientation analyses. The fine-scale microstructures were best observed in the BSE images.

Nanomin analysis was used to locate zircon grains in three representative thin sections (Table 1), which were further investigated by collecting very high-resolution BSE images to characterize zircon grain shapes and internal textures.

2.4 Electron Back Scatter Diffraction (EBSD) Analysis:

EBSD analysis was conducted for selected samples (Table 1) to study the crystallographic orientation of the mineral grains and determine mineral phases and modes. The analysis was used to investigate: (i) crystallographic preferred orientation (CPO), (ii) epitaxy of reactant and product minerals, (iii) 3D connectivity of isolated grains, and (iv) internal deformation of grains typically attributed to dislocation creep.

Crystallographic data for quartz, hornblende, ilmenite, diopside, enstatite, clinozoisite, plagioclase, K-feldspar, apatite, and titanite for the samples were obtained in the XZ plane of the kinematic frame of reference, where 'X' is parallel to the lineation, and 'Z' is oriented normal

to the foliation. There was an exception only for Figure 12 and Figure 13. The XY section was used to maintain the alignment with the 'X' horizontal axis and 'Y' vertical axis of the 3D crystal models. The Oxford Instruments high-resolution EBSD system at the University of Leeds (UK) was used to obtain the data for this project. The thin sections were Syton polished for the analysis (Prior et al., 1996). The operating conditions were 3–4 nA beam current, 25 kV accelerating voltage, 20–25 mm sample distance, and 70° sample tilt in low vacuum mode (40–53 Pa).

Large area EBSD maps were obtained at a step size of 3.5μm and were used to study the grain association and crystal preferred orientation (CPO) over large areas of the thin sections. High-resolution, small area EBSD maps were taken with a step size of 0.7μm. These maps were used to study the detailed crystallographic orientation to observe: 1) epitaxial growth of the minerals, 2) 3D connectivity between the grains, and 3) internal deformation structures such as subgrain boundaries. Indexing of minerals in the EBSD maps was done using the AZtecCrystal software of Oxford Instruments, with an overall percentage of 80–90% of pixels indexed. Prior et al. (2002) was followed for removal of zero solutions and noise reduction.

The EBSD maps and figures presented in this study are as follows: (1) different minerals are represented as color-coded phase maps, (2) Z axis orientation of the minerals is displayed by inverse pole figures (IPF) (same colored grains in the map indicate the same Z axis orientation), (3) gray-scale band-contrast (BC) maps, (4) crystal orientation of the minerals via crystal models generated at specific points in the map (this generates a 3D crystallographic model for the mineral at a specific point), (5) internal lattice distortion typically attributed to dislocation creep through misorientation angle-axis pair, (6) pole figures for the minerals in the XZ section in the lower hemisphere, with an exception for Figure 12 and Figure 13 where the pole figure section is XY. Each of the plots on a pole figure for a particular mineral is the pole of a crystallographic axis of a grain of the respective mineral in the XZ/XY section.

***Table 1**: Methods applied to rock samples. Whole thin section backscattered electron images and photomicrographs (in both plane and crossed polarised light) were collected for all samples listed. These images are available at https://imagematrix.science.mq.edu.au/gallery/ and searching for the keyword 'WFO.' Electron backscattered diffraction (EBSD) maps, and zircon imaging was done for selected samples (tick mark), out of which a few representative samples (double tick mark) are discussed in detail in Chapter 3: Results ('dry' rock samples in **red**; 'wet' rock samples in **green**).*

Sample	Rock type	Assemblage	Large area EBSD map	Small Area EBSD map	Nanomin map	Zircon BSE images
P76569	Pyroxene gneiss	2pyx-pl-kfs-ilm (rare hbl-bt)				
P77350	Pyroxene gneiss	2pyx-pl-kfs-ilm (rare hbl-bt)	✓	✓✓		
9733B	Pyroxene gneiss	2pyx-pl-kfs-ilm (rare hbl-bt)		✓		
9734B	Pyroxene gneiss	2pyx-pl-kfs-ilm (rare hbl-bt)				
P77866	Pyroxene gneiss	2pyx-pl-kfs-ilm (rare hbl-bt)	✓✓	✓✓	✓	✓✓
P77619	Partially hydrated pyroxene gneiss	hbl-bt-cz-pl (low strain)				
9704	(i) Partially hydrated pyroxene gneiss (ii) Hornblende gneiss	(i) cpx with hbl coronae (ii) hbl-bt-cz-pl-ttn	✓✓	✓✓		
P77622	Hornblende gneiss	hbl-bt-cz-pl (high strain)				
9720	Hornblende gneiss	hbl-bt-cz-pl-ttn	✓	✓✓		
9725	Hornblende gneiss	hbl-bt-cz-pl-ttn			✓	✓✓
9703	Hornblende gneiss	hbl-bt-cz-pl-ttn-qz	✓	✓		✓
9710	Hornblende gneiss	hbl-bt-cz-pl-ttn				
P76570	Hornblende gneiss	hbl-bt-cz-pl (high strain)				

Chapter 3: RESULTS

3.1 Whole-rock Geochemistry:

3.1.1 *Major Elements*

Major oxides K_2O, Na_2O, FeO, MgO, CaO, MnO, TiO_2, and Al_2O_3, were plotted on bivariate plots against SiO_2 (Figure 2) for both the 'dry' pyroxene gneiss (i.e., two pyroxene gneisses and all partially hydrated rocks containing relict pyroxene) and 'wet' hornblende gneiss (i.e., all hornblende-rich rocks that lacked pyroxene) in the Western Fiordland Orthogneiss (WFO). For regional reference, data is compared with compiled analyses of the Separation Point Suite.

The first-order observation of the bivariate plots (Figure 2) shows that both the pyroxene and hornblende gneiss components of the Western Fiordland Orthogneiss are more mafic (predominantly SiO_2 < ~57%) compared to the Separation Point Suite (predominantly SiO_2 > ~60%). The two groups form a broad continuous trend across the bivariate plots that overlap in the intermediate ranges of SiO_2 (Figure 2).

There is significant overlap in the bivariate plots for most oxides between the pyroxene and hornblende gneisses of the Western Fiordland Orthogneiss. Although, in general, the hornblende gneisses scatter toward higher SiO_2 and show higher concentrations of K_2O and lower concentrations of CaO at a given SiO_2 (Figure 2).

3.1.2 *Trace Elements*

A range of trace elements for both 'dry' pyroxene gneiss and 'wet' hornblende gneiss were plotted against SiO_2. However, only a few plots (Cr+Ni and Zr) showed significant differences between the pyroxene and hornblende gneisses of the Western Fiordland Orthogneiss (Figure 3). Typically, Cr+Ni is lower, and Zr is higher in the hornblende gneisses compared to the pyroxene gneisses, as observed in the Cr+Ni vs. Zr plot (Figure 3). A bivariate plot of Rb/Sr versus SiO_2 was also plotted to place the geochemical analysis in the context of the major elements. The trace element plots show a continuum between the Western Fiordland Orthogneiss samples and the Separation Point Suite samples, especially for the Rb/Sr plot (Figure 3). The plots further highlight the range of Cr+Ni in the Western Fiordland Orthogneiss compared to the relatively restricted values in the Separation Point Suite.

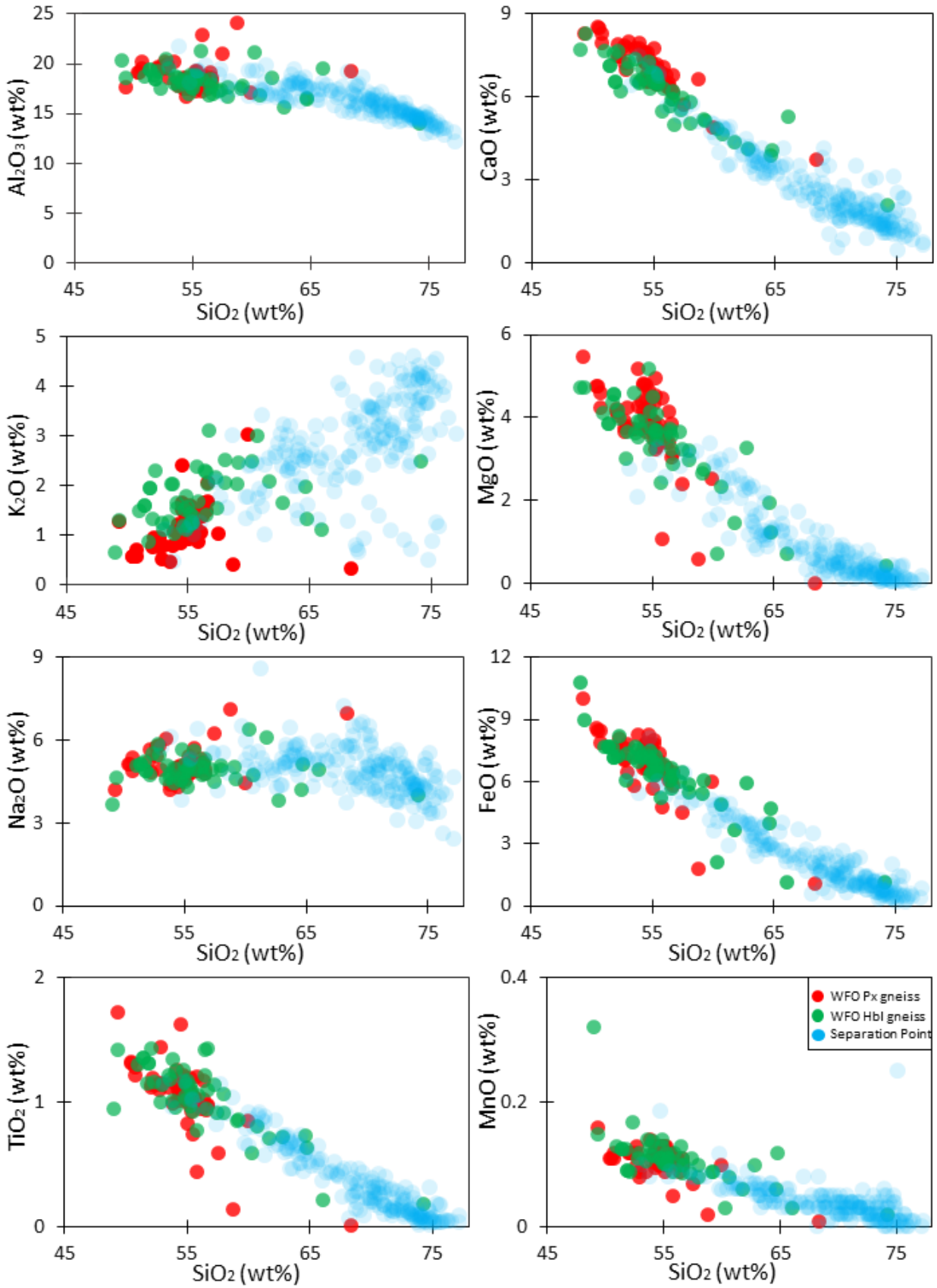

***Figure 2**: Whole rock chemistry (major elements) bivariate plots for the Western Fiordland Orthogneiss (WFO) classified into 1) 'Dry' Pyroxene gneiss (Px gneiss; **red**) and 2) 'Wet' Hornblende gneiss (Hbl gneiss; **green**); and Separation Point Suite (**blue**). Hornblende gneiss data shows (i) enrichment in SiO_2, K_2O and (ii) depletion in CaO compared to pyroxene gneiss. Other major elements are similar between hornblende and pyroxene gneisses.*

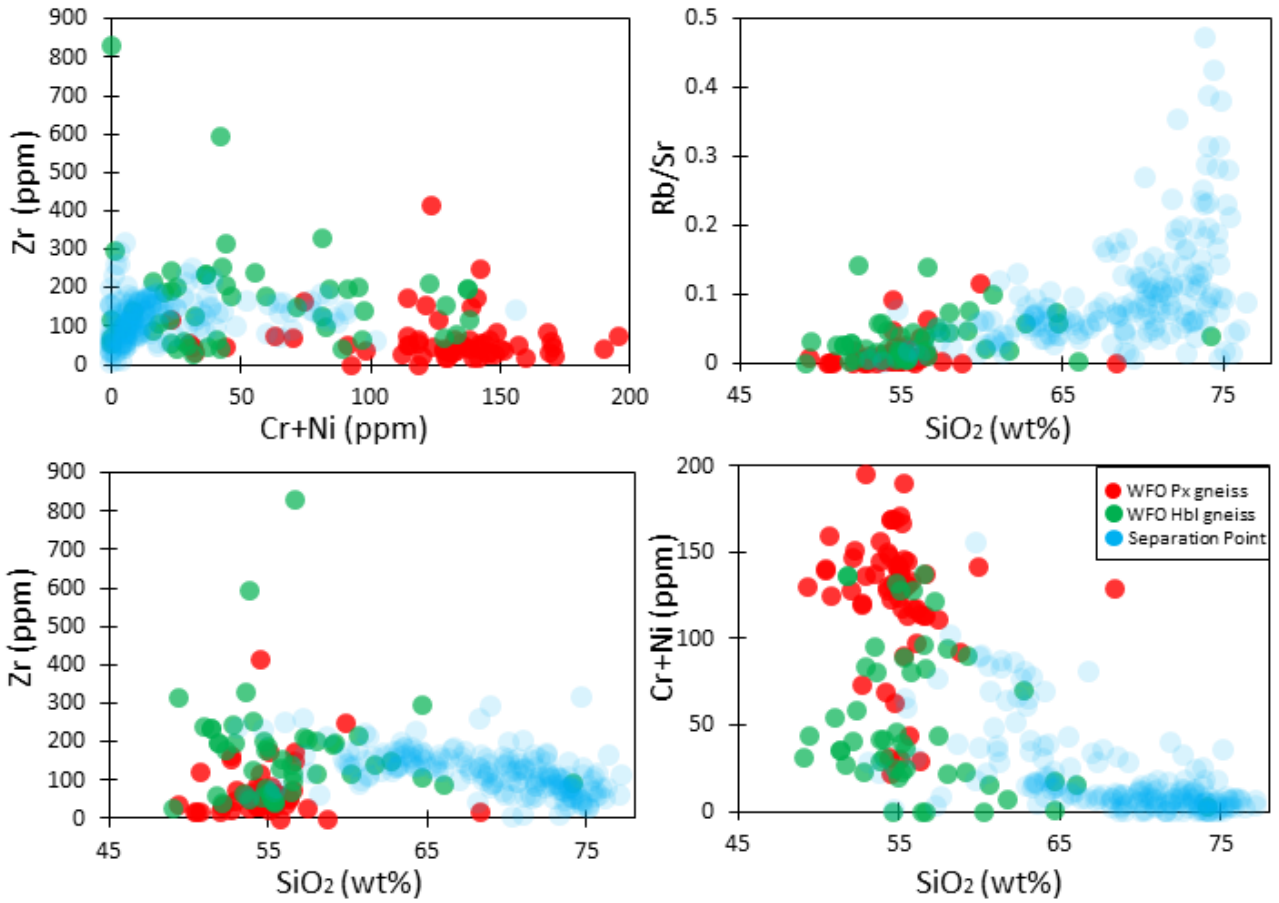

***Figure 3**: Whole rock chemistry (trace elements) bivariate plots for the Western Fiordland Orthogneiss (WFO) classified into 1) 'Dry' Pyroxene gneiss (Px gneiss; **red**) and 2) 'Wet' Hornblende gneiss (Hbl gneiss; **green**); and Separation Point Suite (**blue**). Hornblende gneiss data shows (i) enrichment in Zr and (ii) depletion in Cr+Ni compared to pyroxene gneiss.*

3.2 Field Relationships and Petrography:

Field relationships are briefly summarised from the literature (Allibone et al., 2009; section 1.2; Figure 1) to give context to the petrographic descriptions.

Based on the petrographic analysis, thin sections of thirteen samples of Western Fiordland Orthogneiss from within and adjacent to George Sound Shear Zone were divided into the following classes (samples marked in Figure 1):

(1) **'Dry'** - pyroxene gneiss [samples 9733B, 9734B, P76569, P77350, P77866],

(2) **'Dry'** - predominantly low strain, partially to fully hydrated pyroxene gneiss [samples 9703, 9704(i), P76570, P77619], and

(3) **'Wet'**- hornblende gneiss [samples 9704(ii), 9710, 9720, 9725, P77622].

Representative samples of the classes mentioned above are described in detail below:
P77866 - pyroxene gneiss from the core of Misty Pluton (Figure 1, Figure 4a)
9704 (i) and 9703 - partially to fully hydrated pyroxene gneiss from the margin of the Worsley pluton and McKerr Intrusive near George Sound Shear Zone (Figure 1, Figure 4b)
9704 (ii) and 9720 - hornblende gneiss from the intersection between the George Sound Shear Zone and the McKerr Intrusives (9720 and 9704 marked as 20 and 04 respectively in Figure 1; Figure 4b, 4c).

3.2.1 ***Pyroxene gneiss, P77866***

Sample P77866 (outlined in red Figure 4a) is a two-pyroxene gneiss with a penetrative foliation, representing the predominant rock type central to the Worsley and Misty plutons and the type locality of the western parts of the McKerr Intrusives (marked in red Figure 1). Pyroxene gneiss is remarkably homogenous over kilometer-scale regions of the Western Fiordland Orthogneiss, although the foliation orientation varies across Worsley Pluton, Misty Pluton, and McKerr Intrusives (Allibone et al., 2009).

Sample P77866 is composed of 79% plagioclase feldspar, 8.5% K-feldspar, 4.2% diopside, 3.2% enstatite, and 1.1% ilmenite as the major minerals, and minor (<1%) hornblende, biotite, and quartz. Accessory minerals include apatite and zircon (Figure 4a, Table 2). The minerals are arranged into alternate bands of felsic of about 3 to 4 mm in width (predominantly plagioclase feldspar) and mafic layers of about 1 to 2 mm in width (rich in enstatite and diopside) (Figure 4a).

The coarsest grains in the thin section include both plagioclase and pyroxene grains that are ~2 mm long, while many fine grains are ~200 μm long. Minor grains of ilmenite, hornblende, and biotite are associated with the pyroxene grains, with some occurring in pressure shadows of pyroxene grains (Figure 4a inset). Serrated grain boundaries can be observed in the plagioclase grains (Figure 5e).

3.2.2 ***Low strain, partially to fully hydrated pyroxene gneiss – 9703 & 9704(i)***

These samples represent the peripheral rocks of the Worsley and Misty plutons and the George Sound Shear Zone, particularly in the low-strain parts of the Eastern McKerr Intrusives. The

rocks are heterogeneous over the meter-scale and may enclose isolated remnants of pyroxene gneiss (Allibone et al., 2009; see Figure 1).

Sample 9704 (dashed red & green outline Figure 4b) has two strain domains based on foliation intensity and grain size. The low strain and coarser grained domain is called 9704(i) (upper left of Figure 4b). This domain is composed of 67.8% plagioclase feldspar, 14.4% hornblende, 8.1% diopside, 6.1% biotite, 2.1% titanite, and 1% quartz as the major minerals, and minor (<1%) ilmenite (Table 2). Accessory minerals include clinozoisite (Figure 5f), apatite (Figure 6d), and zircon.

The coarsest grains in this domain include plagioclase (<1.3 mm), diopside (~1.1 mm), and hornblende grains that are up to ~2.3 mm long, while many fine grains in this domain are ~120 μm across. Further, it contains diopside with coronae of symplectic intergrowths of hornblende and quartz (Figure 4b, Figure 5a, Figure 6a). The plagioclase grains show undulose extinction and are associated with fine grains of clinozoisite (Figure 5f). In addition, fine grains of titanite are associated with ilmenite, apatite, and clinozoisite (Figure 6c, 6d). The second domain of 9704(ii) (bottom right of Figure 4b) is described in section 3.2.3.

Sample 9703 is also representative of the fully hydrated pyroxene gneiss group. It comprises 54.4% plagioclase feldspar, 22.4% hornblende, 11.0% biotite, 7.8% quartz, 2.3% titanite, and 2.1% clinozoisite as the major minerals, and minor (<1%) K-feldspar. Accessory minerals include apatite and zircon (Table 2).

Samples 9704(i) (Figure 4b) and 9703 (can be found in Imagematrix) are two representative examples of the heterogeneous group, which is distinguished by the presence of hornblende-quartz intergrowths. These intergrowths may form coronae around corroded pyroxene (most commonly diopside as shown in 9704(i) (Figure 4b, Figure 5a, Figure 6a) but are more commonly observed as complete pseudomorphs of inferred former pyroxene (Figure 4b inset, Figure 5b, 5c). Penetrative foliation from the pyroxene gneiss is now defined by elongate mafic clusters of hornblende-quartz-biotite (± clinozoisite) (Figure 4b; Figure 5c, 5d, 5f). However, minerals within each cluster are generally poorly aligned in these rocks (Figure 5c).

3.2.3 ***Hornblende gneiss – 9704(ii) and 9720***

These samples represent the rocks of the western margin of Worsley, the eastern margin of Misty plutons along the George Sound Shear Zone, and the eastern McKerr Intrusives. These rocks are hornblende gneisses (marked in green in Figure 1; Allibone et al., 2009).

Sample 9704(ii) (Figure 4b) and sample 9720 (outlined in green Figure 4c) are representative examples of this group which is distinguished by a penetrative foliation defined by aligned hornblende, biotite, and clinozoisite. Sample 9720 comprises 52.2% plagioclase feldspar, 18.8% hornblende, 10.6% biotite, and 2.3% clinozoisite, 1.1% titanite as the major minerals, and minor (<1%) K-feldspar, quartz (Table 2). Accessory minerals include apatite and zircon. This group contains the coarsest grain sizes in the study.

The coarsest grains in the thin section include plagioclase (~4.8 mm), biotite (~3 mm), and hornblende (~2.7 mm) grains, while clinozoisite is also coarse (~1 mm) (Figure 5g). Many fine grains are ~100 μm across. The mafic minerals define the prominent foliation (~3 mm in width) that may anastomose around domains rich in plagioclase feldspar (Figure 4c) to form a pattern similar to an S-C' fabric. Some plagioclase grains include many euhedral crystals of fine clinozoisite (~0.2 mm) (Figure 4c).

To summarise the petrographic study, diopside is observed to be partially replaced by hornblende, quartz, and biotite. In some areas, pyroxene is completely replaced by hornblende-quartz symplectite and biotite, while hydration of plagioclase to form clinozoisite also increases in prevalence. The strongest foliation intensity is observed in the hornblende gneiss, which also presents the coarsest grain sizes.

***Table 2**: The modal percentage of minerals in the thin sections for samples P77866, 9704 (9704(i) & 9704(ii) belong to the same slide), 9703, 9720 discussed in section 3.2. ('dry' samples in **red**; 'wet' samples in **green**). The sample locations are marked in Figure 1. The modal percentages are calculated using Image J software.*

Minerals	**P77866 Pyroxene gneiss**	**9704 Hydrated Pyroxene gneiss**	**9703 Fully hydrated Pyroxene gneiss/ Hornblende gneiss**	**9720 Hornblende gneiss**
Plagioclase	79%	67.8%	54.4%	52.5%
K-feldspar	8.5%	<1%	<1%	<1%
Diopside	4.2%	8.1%	-	-
Enstatite	3.2%	-	-	-
Ilmenite	1.1%	<1%	-	-
Hornblende	<1%	14.1%	22.4%	18.8%
Biotite	<1%	6.1%	11%	10.6%
Quartz	<1%	1%	7.8%	<1%
Titanite	-	2.1%	2.3%	1.1%
Clinozoisite	-	<1%	2.1%	2.3%
Apatite	<1%	<1%	<1%	<1%
Zircon	<1%	<1%	<1%	<1%

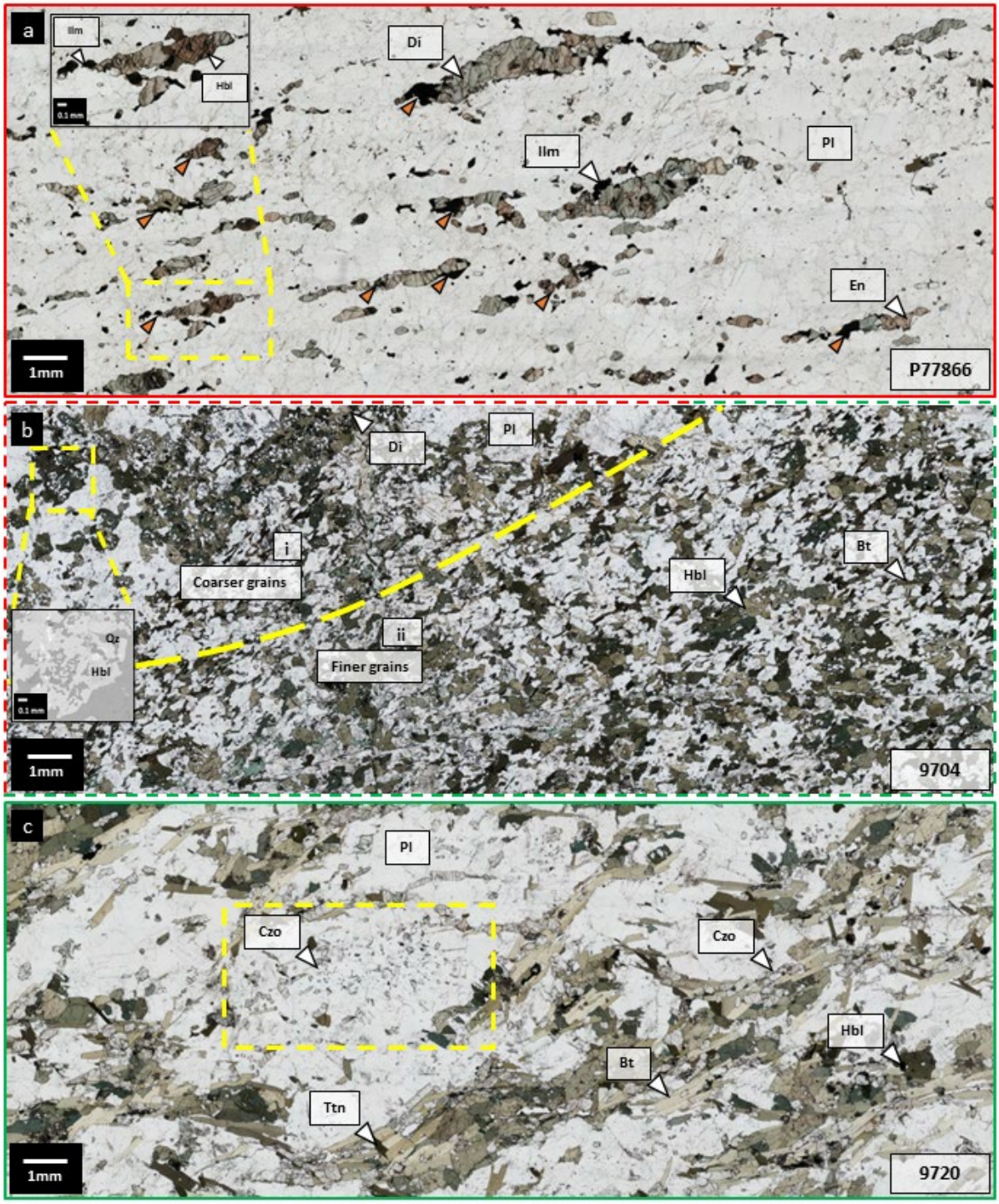

Figure 4: *Overview photomicrographs of the Western Fiordland Orthogneiss (WFO) across the George Sound Shear Zone: (a) P77866: coarse-grained pyroxene gneiss (**red box**) highlighting alternate felsic & mafic bands. The felsic band is predominantly comprised of plagioclase (Pl), whereas the mafic band is rich in enstatite (En), diopside (Di), and ilmenite (Ilm) grains; Inset shows that ilmenite (**orange arrows**) occurs in strain shadows; (b) 9704: partially hydrated (**red dashed line**, upper left) to fully hydrated (**green dashed line**, lower right) pyroxene gneiss (separated by **yellow dashed line**) with diopside, hornblende (Hbl), biotite (Bt), and plagioclase; Inset showing symplectites of hornblende and quartz pseudomorphing diopside (yellow dashed box) and progressive grain size fining (across yellow dashed line); NOTE domains labeled (i) & (ii). (c) 9720: hornblende gneiss (**green box**) comprised of hornblende, biotite, clinozoisite (Czo), and minor apatite and titanite, alternating with plagioclase-rich domains. The modal proportion of hydrous minerals increases from Pyroxene Gneiss (a) to Hornblende Gneiss (c).*

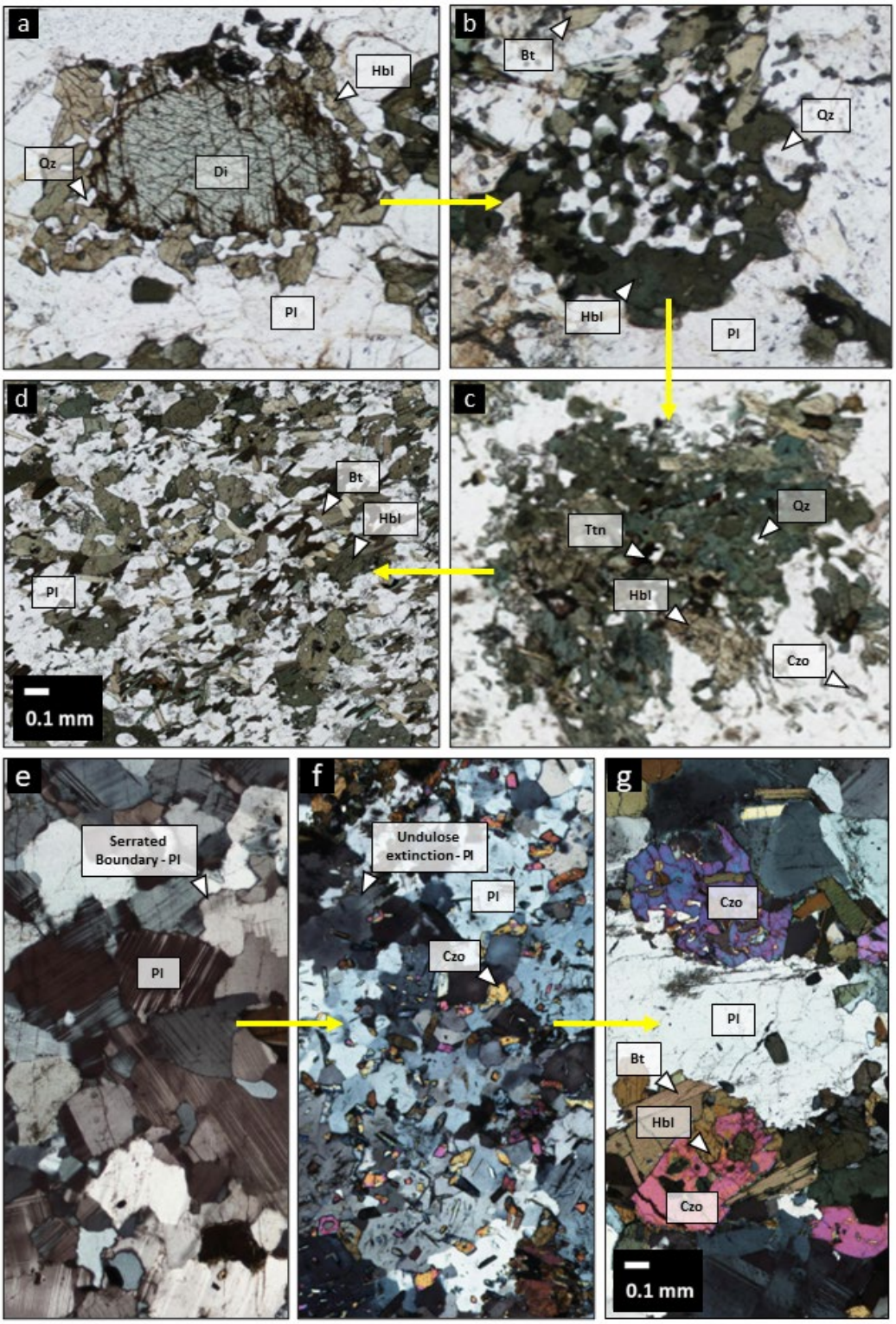

***Figure 5**: **a to d**: Plane polarized light (PPL) photomicrographs showing reaction textures; (a) 9704: diopside (Di) partially replaced by a symplectite of hornblende and quartz; (b) 9704: diopside completely pseudomorphed by hornblende and quartz; (c) 9703: grain size reduction and diopside completely pseudomorphed by hornblende, biotite, titanite, and quartz; (d) 9704: foliated finer grains of hornblende, biotite, and plagioclase, showing phase mixing. **e to g**: Crossed polarized light (XPL) photomicrographs of (e) P77866: plagioclase with serrated boundaries in pyroxene gneiss; (f) 9703: finer grains of clinozoisite within plagioclase, undulose extinction in plagioclase in the partially to fully hydrated pyroxene gneiss; (g) 9720: coarser grains of clinozoisite in hornblende gneiss. The **yellow arrows** point towards the direction of increasing modes of the hydrous minerals in a to d and e to g.*

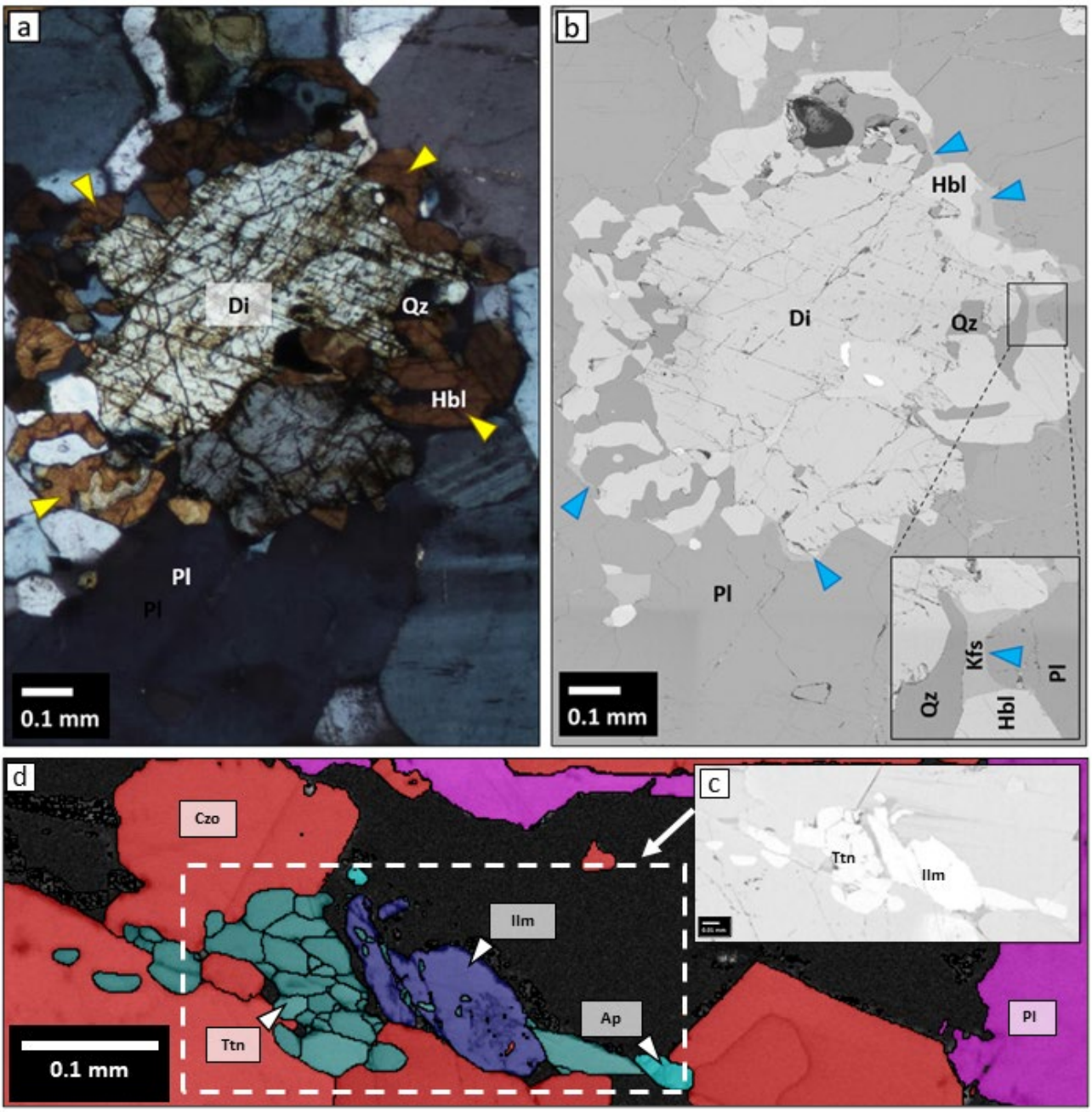

***Figure 6**: Reaction textures in sample 9704 showing: (a) crossed polarized light (XPL) photomicrograph of a symplectic corona of hornblende and quartz around diopside and some hornblende grains with similar extinction angle (**yellow arrows**); (b) Backscattered electron (BSE) image showing fine interstitial elongate K-feldspar grains within the corona texture (**blue arrows**), (c) BSE image showing titanite and ilmenite, both with bright back-scattered electron response, (d) Electron backscattered diffraction (EBSD) phase map showing a clearer distinction of minerals in the assemblage of ilmenite, titanite, clinozoisite, and apatite (note: biotite poorly indexed and is shown as dark grey). The ilmenite grain is corroded and rich in inclusions, with titanite inferred as the reaction product.*

3.3 Backscattered Electron Image Analysis:

High-resolution backscattered electron images show fine-scale microstructures (Figure 6b, Figure 6c, Figure 7, Figure 8) that cannot be resolved by investigation under a petrographic microscope.

Backscattered electron images show the following microstructures in 'dry' pyroxene gneisses (in a red box in Figure 7, Figure 8): (i) irregular-shaped grains of ilmenite, quartz, and K-feldspar (Figure 6b; green arrows: Figure 7), (ii) low dihedral angles subtended by quartz and K-feldspar between surrounding grains (red arrows: Figure 7), (iii) elongate interstitial grains of quartz and K-feldspar (blue arrows: Figure 7, Figure 8), and (iv) cuspate grain boundaries in K-feldspar and ilmenite (yellow arrows: Figure 7). Elongate grains of K-feldspar occur within the corona structure of hornblende and quartz around pyroxene (Figure 6b). In addition, zircon is observed in two textural settings: (a) forming very fine grains (~1 μm) and zircon films (~1 μm thick) at the margins of oxide minerals (orange arrow: Figure 8), (b) as irregular-shaped grains of zircon (~50 μm) that have patchy micron-scale porosity when observed at a higher resolution (orange arrows: Figure 8), and (c) curvilinear boundary in zircon (yellow arrow: Figure 8). A visual estimate of the area comprising melt pseudomorphs is less than 1%.

Similarly, microstructures in 'wet' hornblende gneisses (in a green box in Figure 7, Figure 8) include: (i) irregular-shaped grains of quartz and K-feldspar (green arrow: Figure 7, Figure 8), (ii) low dihedral angles subtended by quartz and K-feldspar (red arrow: Figure 7) between surrounding grains, (iii) elongate grains of ilmenite and quartz (blue arrow: Figure 7, Figure 8), and (iv) cuspate grain boundary observed in quartz and K-feldspar (yellow arrow: Figure 7). Zircon grains are coarser (~ 80 μm) compared to those in the pyroxene gneisses. Coarser zircon grains are irregularly shaped with curvilinear boundaries (yellow arrow: Figure 8) and have porosity trails or dissolution channels within the grains (orange arrows: Figure 8). Smaller zircon grains (~40μm) show well-faceted boundaries and lack evidence for dissolution processes affecting them (Figure 8). A visual estimate of the area comprising melt pseudomorphs is less than 2%.

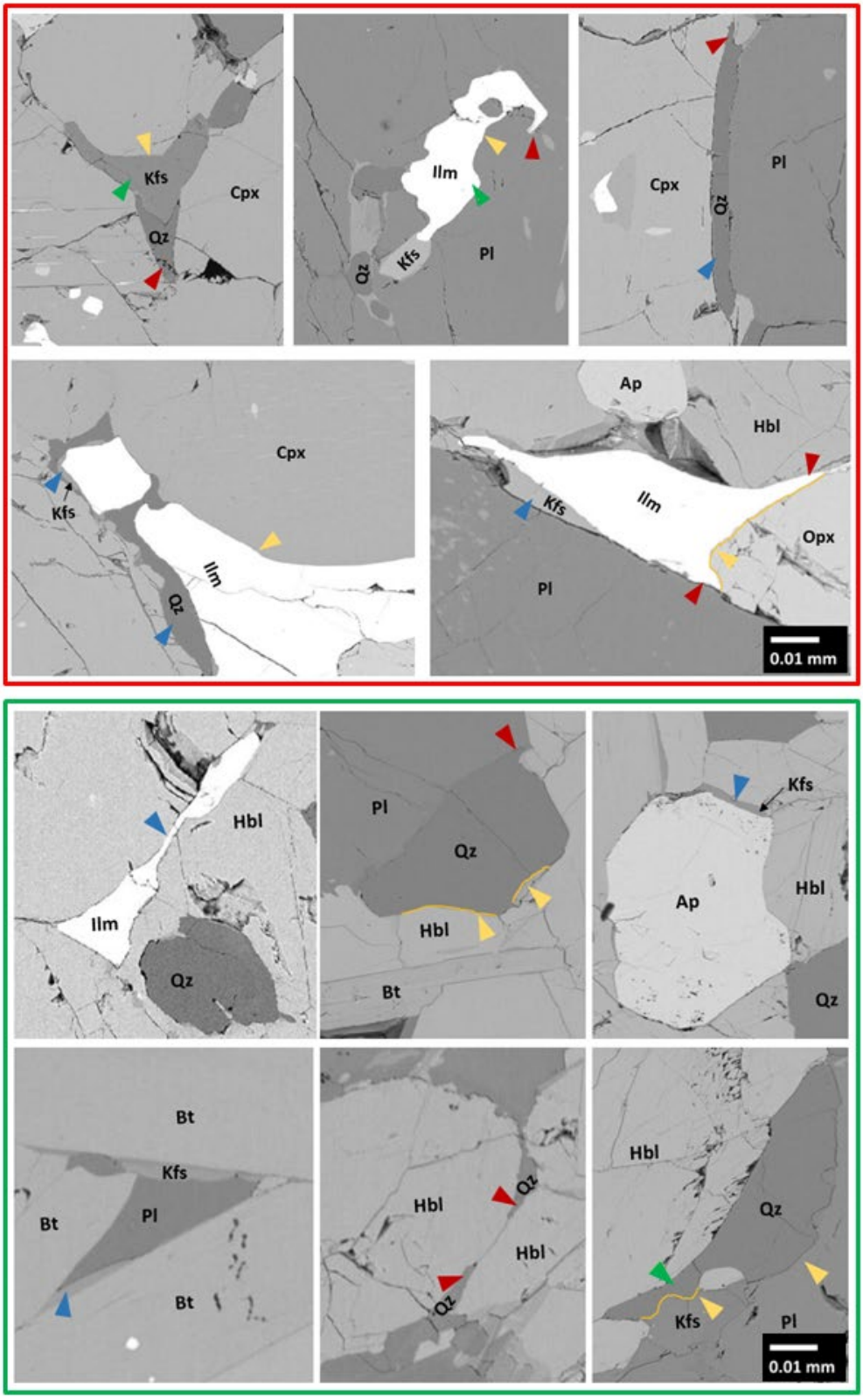

Figure 7**: Backscattered electron images showing textures in pyroxene gneiss samples P77866 & P77619* ***(red box): *indicating low dihedral angles in quartz and ilmenite (**red arrows**); interstitial grains and films of quartz, K-feldspar around minerals (**blue arrows**); irregular-shaped grains of ilmenite and K-feldspar (**green arrows**); cuspate grain boundaries (**yellow arrows**); Backscattered electron images showing textures in hornblende gneiss samples 9720 & P76570* ***(green box):*** *indicating low dihedral angles in quartz (**red arrows**); interstitial grains and films of ilmenite and K-feldspar (**blue arrows**); irregular shaped grains of quartz (**green arrows**); cuspate grain boundaries (**yellow arrows**).*

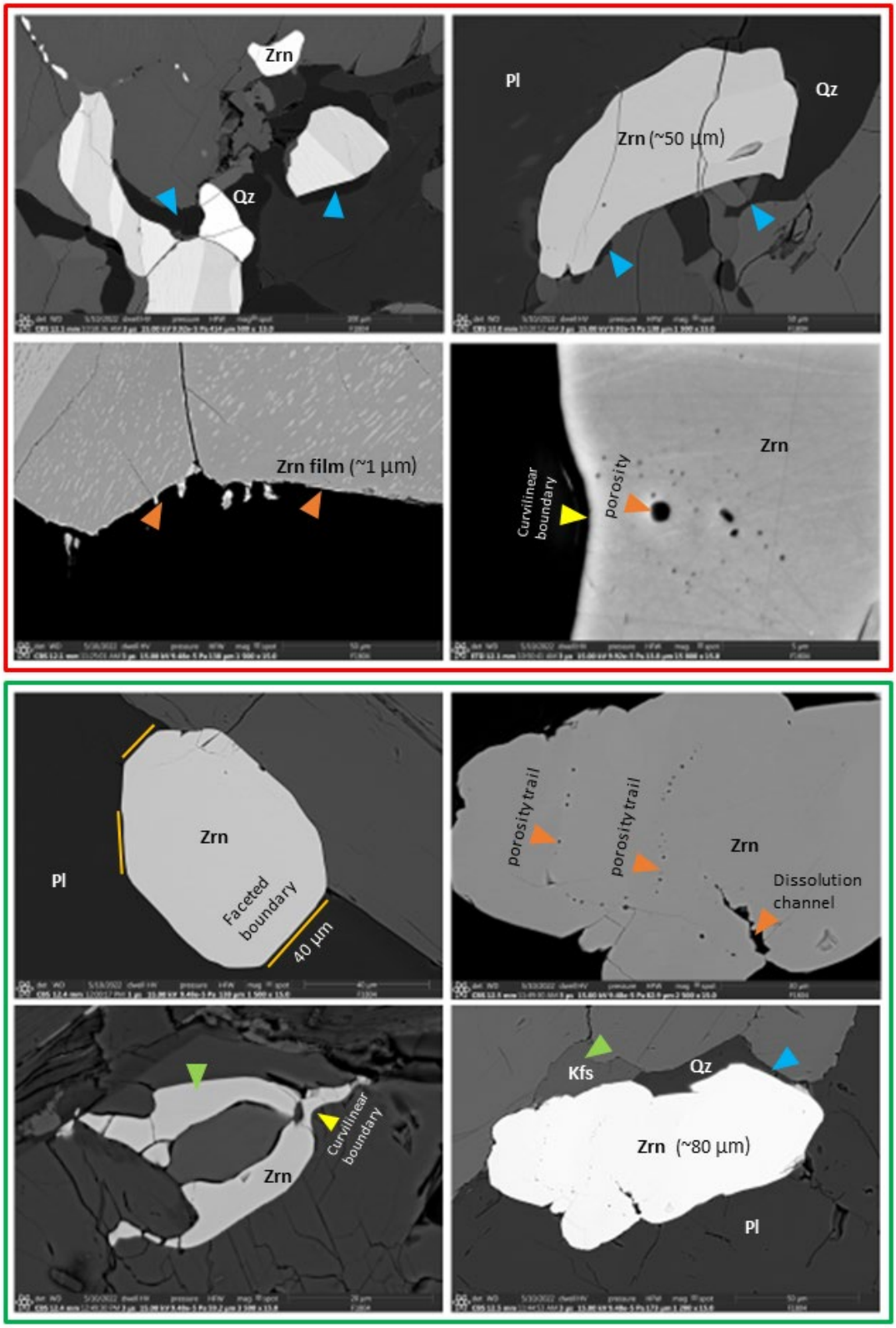

Figure 8: *Backscattered electron images showing zircon textures in pyroxene gneiss sample P77866* ***(red box):*** *zircon films on oxide grains and porosity in zircon (**orange arrows**); interstitial grains of quartz adjacent to zircon (**blue arrows**); the curvilinear boundary of zircon (**yellow arrows**); Backscattered electron images showing textures in hornblende gneiss sample 9725* ***(green box):*** *well-faceted fine-grained zircon grains; porosity trails, dissolution channels in coarse-grained zircon (**orange arrows**); interstitial grains of quartz (**blue arrows**); curvilinear boundaries of zircon (**yellow arrows**); irregular grains of zircon and associated K-feldspar (**green arrows**).*

3.4 Electron Back-Scatter Diffraction (EBSD) Analysis: Quantitative orientation data

Electron backscatter diffraction (EBSD) analysis is used to determine the degree to which minerals display a crystal-preferred orientation at the thin section scale and to examine how this relates to the gneissosity. Additionally, orientation data is used to identify (i) where the crystal orientation of product minerals is controlled by the minerals that have been partially replaced (i.e., epitaxy), (ii) interconnectivity of interstitial minerals in three dimensions (3D connectivity), and (iii) lattice distortions within grains (e.g., subgrain formation).

3.3.1 *Crystal Preferred Orientation (CPO)*

Crystal preferred orientation of the minerals can be observed in the pyroxene gneiss. As the modal proportion of pyroxene decreases and hornblende increases, the hornblende grains show a stronger crystal preferred orientation (CPO) (Supplementary Figure i, ii, iii, iv). A cluster in the misorientation angle-axis plot for a low angle axis for hornblende is seen in sample P77866, but as the hornblende proportion increases in sample 9704, no cluster for a low angle axis is observed (Supplementary Figures i, ii, iii, iv).

3.3.2 *Epitaxy between minerals*

Hornblende shows similar crystal axis orientation (i.e., epitaxy) along the {100} and {010} axis with the relict pyroxene minerals - enstatite and diopside in pyroxene gneiss (pole figure XZ section; Figure 9). In addition, the {0001} axis of the quartz grains show partial epitaxy with the {010} axis of both hornblende, with which they are intergrown, and pyroxene, which they partially replace. As the modal proportion of pyroxene grains reduces in the samples and hornblende increases, the epitaxy between the pyroxene and hornblende grains is consistent (pole figure XZ section; Figure 10, Figure 11). However, the epitaxy cannot be observed in the hornblende gneisses due to the complete absence of the pyroxene grains.

3.3.3 *3D-connectivity within grains*

Hornblende, ilmenite, and quartz grains show 3D connectivity in the pyroxene gneiss. As can be observed (crystal models: Figure 12), the three axes are aligned in 3D in grains that are separate from each other in the 2D map. As the modal proportion of pyroxene grains reduces and the hornblende grains increases, the 3D connectivity can be observed in hornblende and quartz (crystal models; Figure 13).

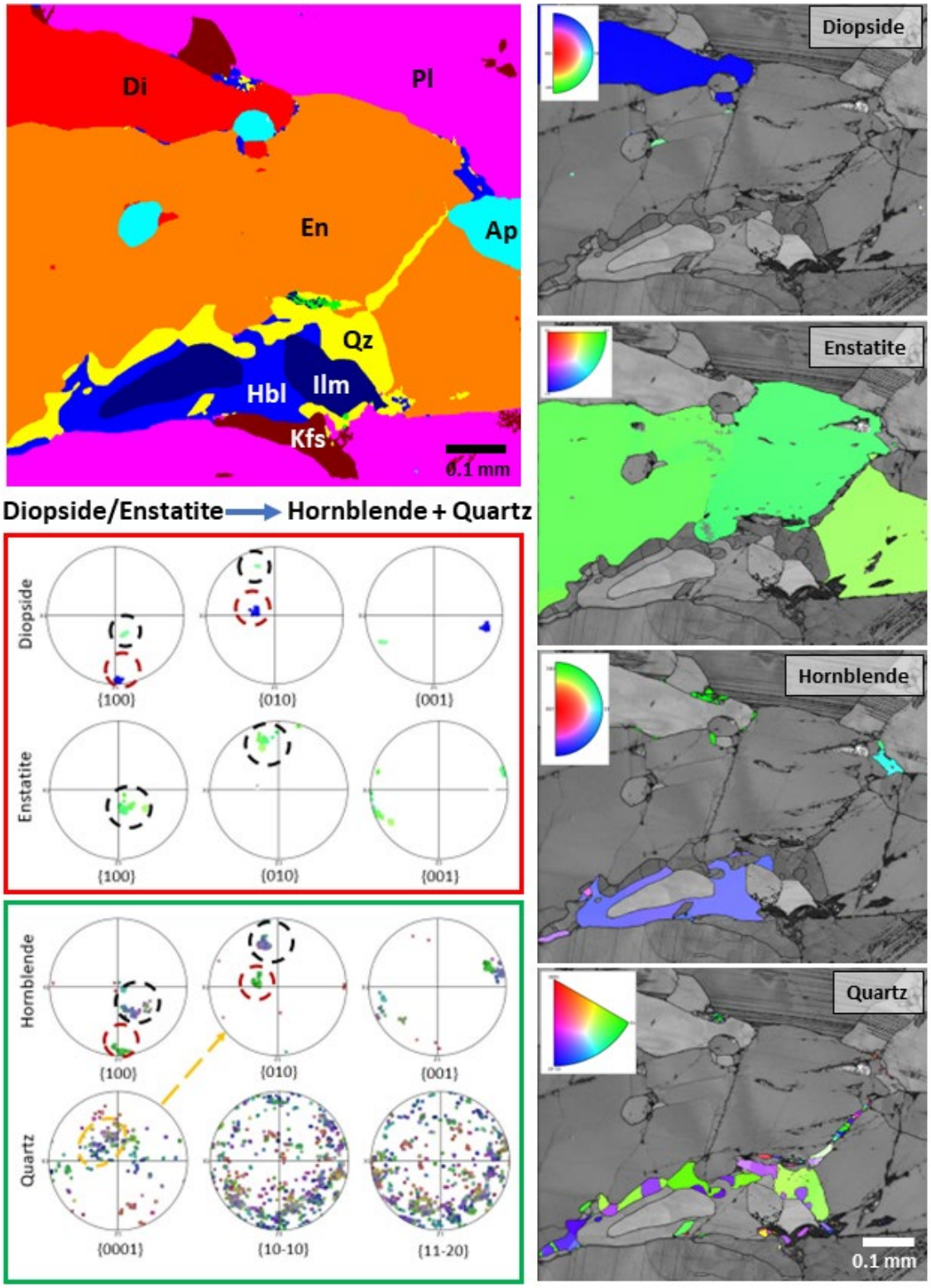

Figure 9: *EBSD Map of sample P77866 showing,* ***Vertical panel to the right****: Z-axis Inverse Pole Figure (IPF) maps for the minerals with the band contrast image in the background (top to bottom) - diopside, enstatite, hornblende, and quartz (patches of alternate colors in quartz grains, e.g., purple and green color indicate twinning in quartz grains).* ***Vertical panel to the left****: 1) Phase map for all the minerals, 2) the mineral reaction, 3) XZ Pole figures for diopside, enstatite, hornblende, and quartz. The color of crystallographic axes plots of the minerals corresponds to the IPF coloring of the grains of the respective minerals in the right panel. The* ***red box*** *indicates the pole figures for reactant minerals and the* ***green box*** *for product minerals. (see supplementary figure v for pole figures at a bigger scale).*

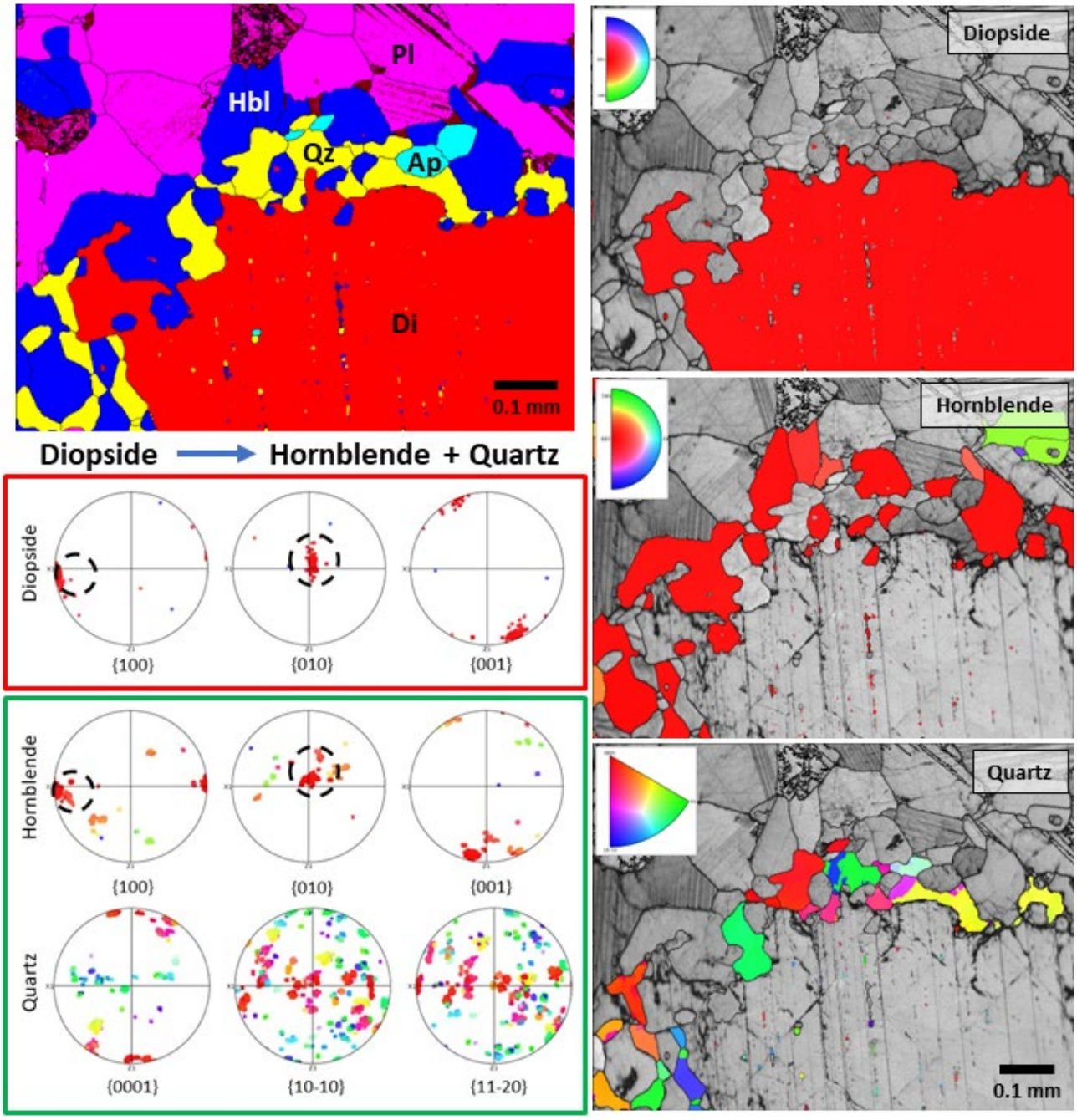

Figure 10: *EBSD Map of sample 9704 showing,* ***Panel to the right****: Z-axis Inverse Pole Figure (IPF) maps for the minerals with the band contrast image in the background (top to bottom) - diopside, hornblende, and quartz (domains of alternate color in the same grain indicate twinning in quartz grains).* ***Panel to the left****: 1) Phase map for all the minerals, 2) the mineral reaction, and 3) XZ Pole figures for the minerals diopside, hornblende, and quartz. The color of the crystallographic axis of plots for minerals in the pole figure corresponds to the IPF coloring of the grains of the respective minerals in the right panel. The* ***red box*** *indicates the pole figures for reactant minerals and the* ***green box*** *for product minerals (see supplementary figure vi for pole figures at a larger scale).*

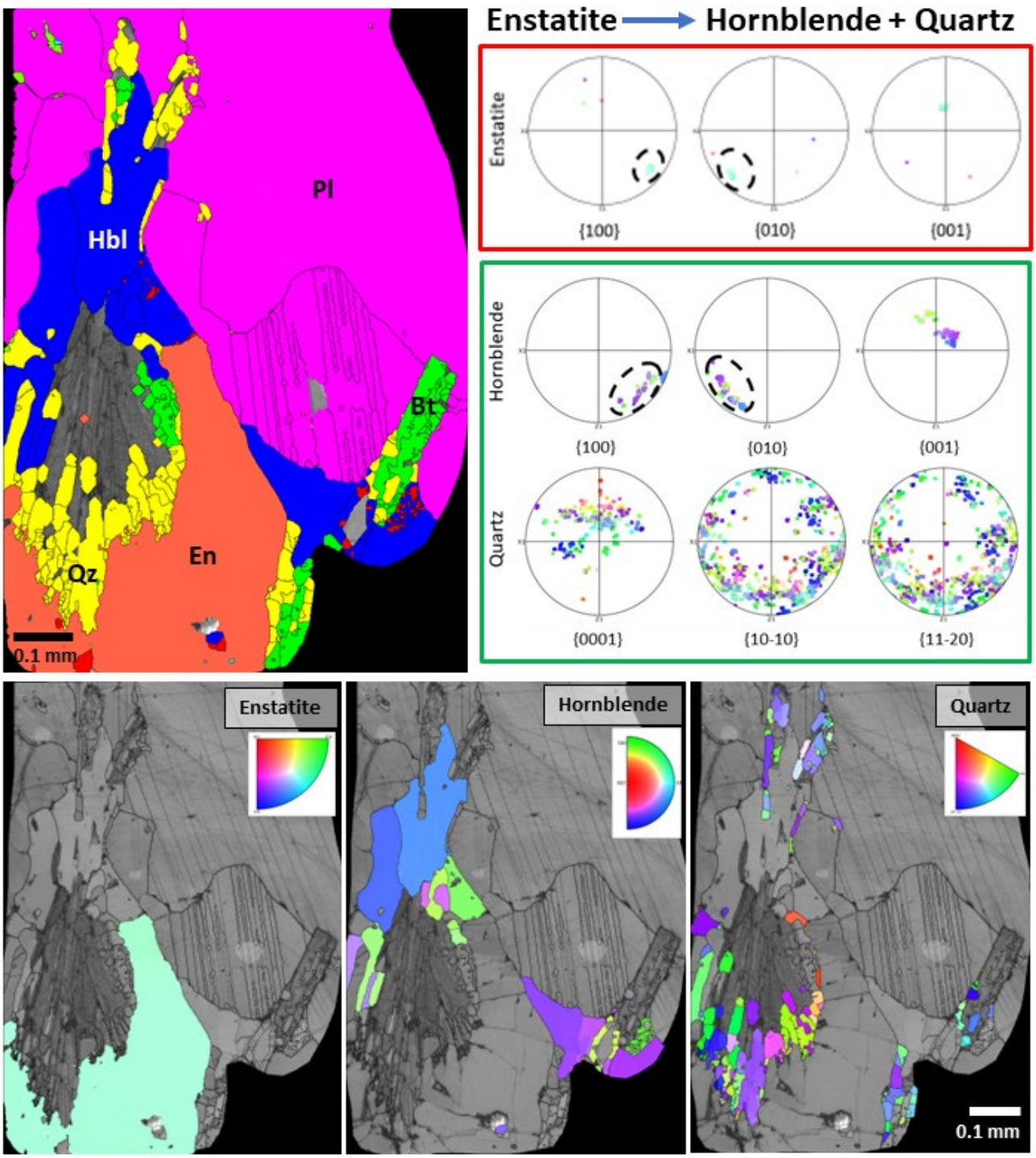

Figure 11: *EBSD map of sample P77350 showing,* ***Top left****: Phase map for all the minerals;* ***Top right****: The mineral reaction followed by XZ Pole figures for the minerals enstatite, hornblende, and quartz. The color of crystallographic axis plots of minerals in the pole figure corresponds to the Inverse Pole Figure (IPF) coloring of the grains of the respective minerals at the bottom. The* ***red box*** *indicates the pole figures for the reactant minerals and the* ***green box*** *for the product minerals (see supplementary figure vii for images of pole figures at a larger scale);* ***Bottom (left to right)****: Z-axis IPF maps for the minerals, enstatite, hornblende, and quartz with band contrast image in the background (domains of alternate color in the same grain indicate twinning in quartz grain).*

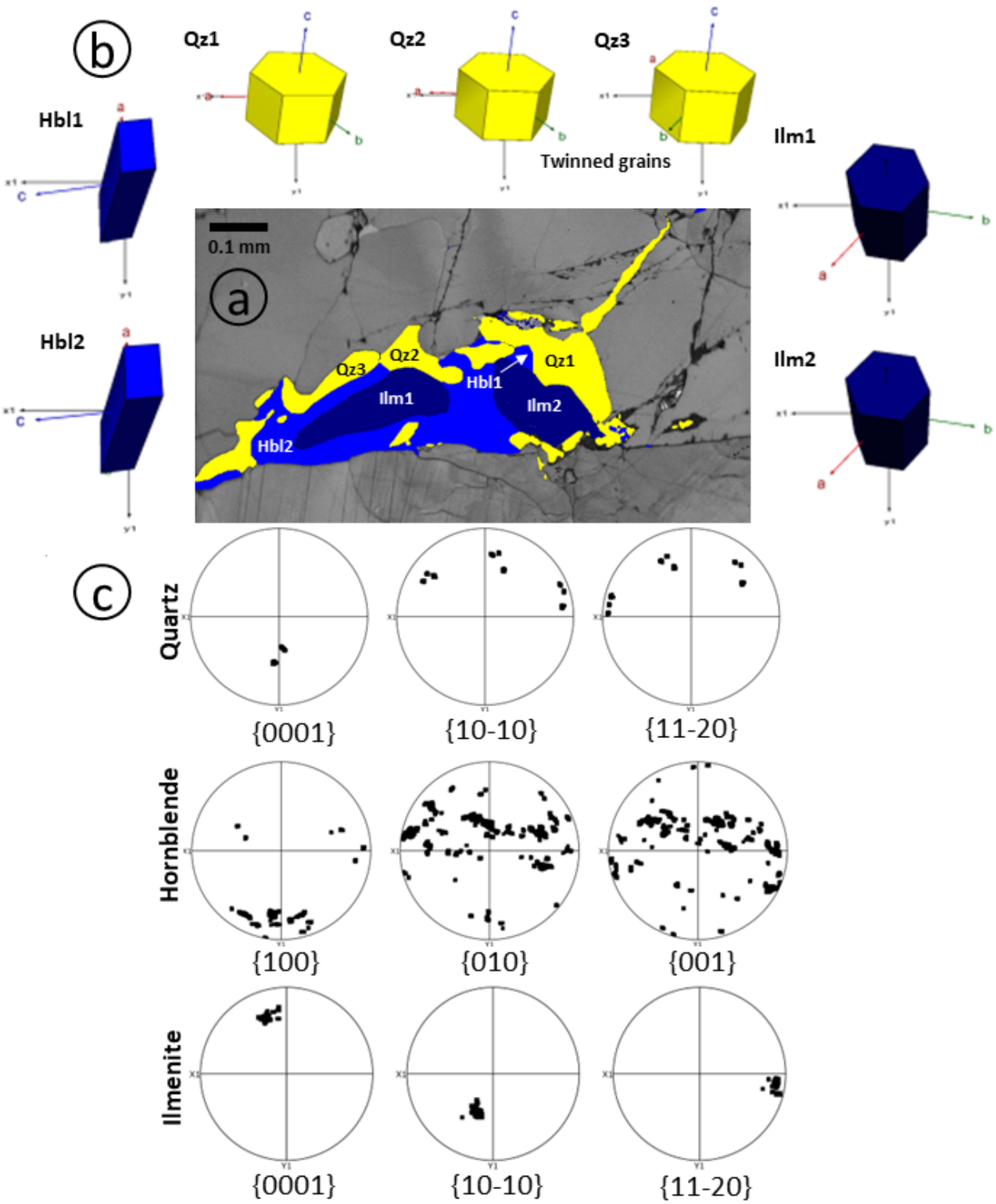

Figure 12: *EBSD Map of P77866 showing: a)* ***Phase map*** *of the minerals with points marked for the crystal orientation (e.g., Qz1, Qz2, Qz3); b)* ***3D models*** *of the crystals at specific points demonstrating 3D connectivity of the grains of quartz (Qz), hornblende (Hbl), and ilmenite (Ilm), and c)* ***XY pole figures*** *for the mineral axis plots showing clustering for the three crystal axis. The spread in the plot for quartz is due to twinned grains; the spread in the plot for hornblende is due to the very fine grains which form a cluster for the crystallographic axis.*

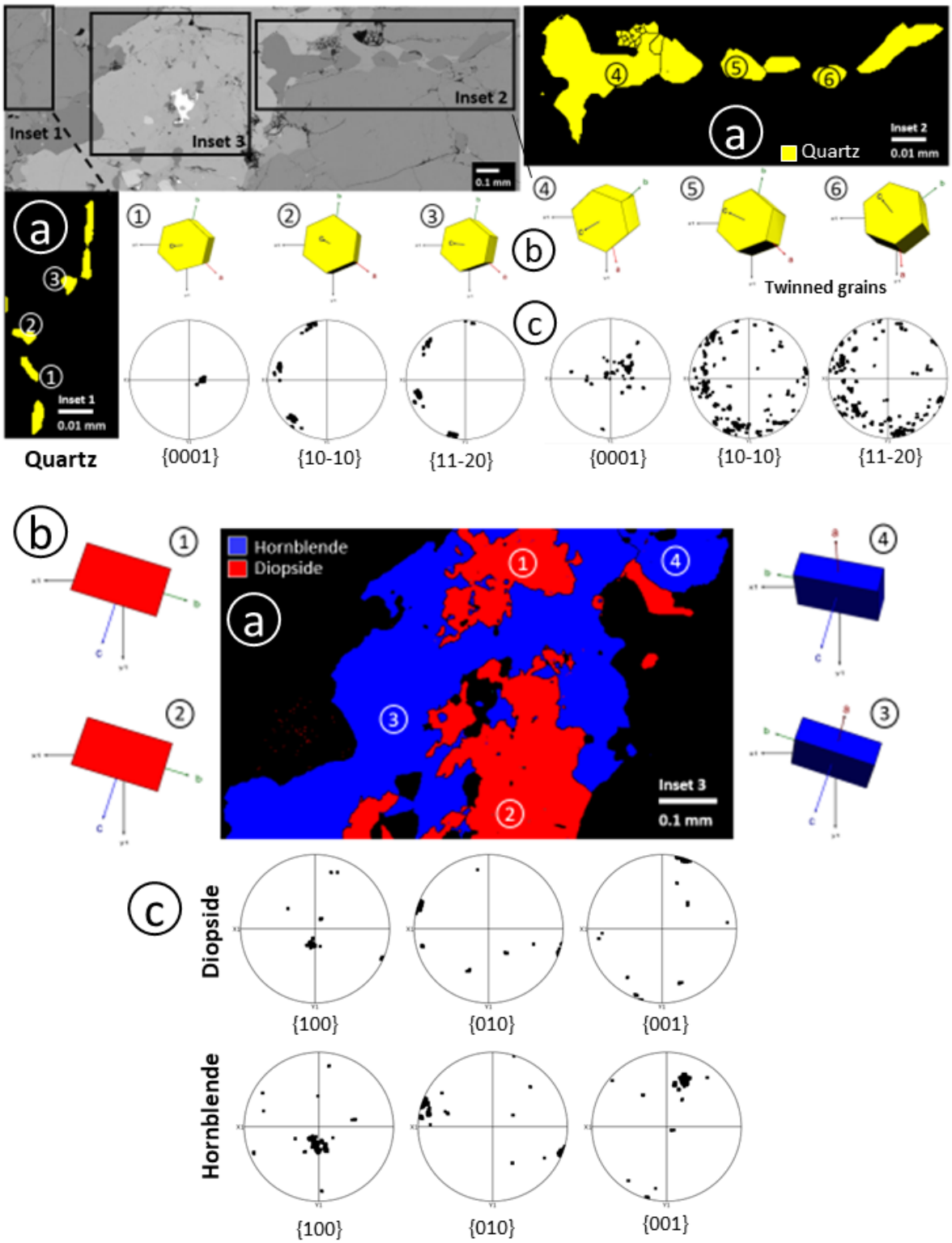

Figure 13: *EBSD Map of P77350 showing, a)* ***Phase map*** *of the minerals with points marked for the crystal orientation (e.g., marked as 1,2,3 on quartz grains, inset 1), b)* ***3D models*** *of the crystals (e.g., marked as 1,2,3 for quartz grains, inset 1) for corresponding points marked on grains demonstrate 3D connectivity of the grains of quartz, hornblende, and diopside, Points 4,5,6, for quartz in inset 2 have the same orientation but are twinned grains; relict grains of diopside in inset 3 show 3D connectivity as they were once part of a single grain, product mineral hornblende in inset 3 not only show 3D connectivity but also epitaxy with relict diopside; and c)* ***XY pole figures*** *show clustering for the three crystal axis for minerals in inset 1,2,3; the difference in cluster position for {001} axis for hornblende and diopside is due to differences in crystallography.*

Chapter 4: DISCUSSION

It is proposed that the pyroxene gneiss of the Western Fiordland Orthogneiss has been fluxed by melt moving through the George Sound Shear Zone, which accounts for the hornblende gneiss found in the area. In the following sections, the evidence for melt flux during deformation in the George Sound Shear Zone is examined, and the implications for melt pathways in the lower crust discussed.

4.1 Evidence for the former presence of melt in all rocks studied

Backscattered electron (BSE) images show quartz, K-feldspar, and ilmenite (Figure 6b, Figure 7, Figure 8) grains subtending low dihedral angles between the surrounding grains. Interstitial irregular grains of quartz, K-feldspar, and ilmenite in the BSE image lack well-developed crystal facets (Figure 7, Figure 8). Elongate grains of quartz and K-feldspar with a high aspect ratio can be seen as 'films' along grain boundaries (Figure 6b, Figure 7). Cuspate grain boundaries are observed for quartz, K-feldspar, and ilmenite (Figure 7). These textures are found in the 'dry' pyroxene gneisses, as well as the 'wet' hornblende gneisses. They are interpreted to be pseudomorphs of a former melt that migrated along the grain boundaries (Harte et al., 1991; Holness and Sawyer, 2008; Marchildon and Brown, 2002; Rosenberg and Riller, 2000; Sawyer, 1999; Sawyer, 2001; Vernon, 2011) and are indicative of the former presence of melt (see also section 1.1.2).

An association of fine grains of elongate (high aspect ratio) K-feldspar with symplectite of hornblende and quartz forming corona around pyroxene grains can be observed (Figure 5a, Figure 6b). This textural evidence indicates that K-feldspar grains crystallized from a former melt that was present during the formation of hornblende and quartz corona around pyroxene grains. Finer zircon grains with well-developed facets in the hornblende gneiss (Figure 8) and the presence of porosity trails and dissolution channels in the coarser zircon grains in the pyroxene gneiss and hornblende gneiss (Figure 8) can be observed. These textures in zircon indicate that the crystals have been subjected to coupled dissolution-precipitation (CDP) in the presence of a melt and corresponding reaction (Halpin et al., 2020; Corfu et al., 2003). Further, the zircon grains are associated with interstitial grains of quartz, and K-feldspar, which are also interpreted to have crystallized from a former melt (Figure 8).

Although textures indicative of former melt are also typical of igneous rocks, their association with the reaction coronae around pyroxene (Figure 6) and porosity channels caused by crystal dissolution-precipitation (CDP) in zircon (Figure 8) attests to a metamorphic origin for at least some of the hornblende-rich rocks. Similar textures indicative of the former presence of melt can be observed in the pyroxene gneiss (including partially hydrated pyroxene gneisses) as well as the hornblende gneisses (Figure 6, Figure 7). Hence, it can be interpreted that at least some of the metamorphism of the Western Fiordland Orthogneiss was driven by melt-rock interaction.

A misorientation axis-angle pair plot shows a cluster of low angle axis for the hornblende grains in the least hydrated sample of pyroxene gneiss (Supplementary Figure i) which indicates potential internal crystal lattice distortion of the grains. With the increasing modal proportion of hydrous minerals in the pyroxene gneiss, there is no observable clustering of low angle axis in the misorientation plot for hornblende (Supplementary Figure ii, iii), indicating negligible internal deformation within grains. Grains with negligible internal crystal lattice distortion forming in rocks in the high strain zone might be possible if there is melt in the system that accommodates the strain (Stuart et al., 2016; Stuart et al., 2017; Stuart et al., 2018). Hence, it can be inferred that there was melt in the system, which accommodated the strain during the formation of hornblende grains as hydration progressed in the pyroxene gneisses in and around the George Sound Shear Zone.

A very similar crystallographic orientation for multiple nearby small grains of quartz, ilmenite, and hornblende is identified in the EBSD maps (Figure 12, Figure 13). It can be inferred that although not connected in the 2D section, these grains are connected in 3D (Figure 12, Figure 13), forming branching grains that pseudomorphed grain boundary networks of melt. These branching grains are common in igneous rocks. They are inferred to form during the final crystallization of the small proportions of melt that remain along grain boundaries and at grain junctions as the rock solidifies (Holness, 2006, Holness & Sawyer, 2008). However, it is consistently observed that there are 3D connected grains of quartz and hornblende throughout the textural progression of hydration documented in this study, as the 'dry' pyroxene gneisses (Figure 12) transition to 'wet' hornblende gneisses (Figure 13). Hence it can be interpreted that melt-rock interaction led to the progression of pyroxene gneiss to hornblende gneiss.

4.2 Open system melt-rock reactions, geochemical changes (metasomatism), and inferred melt composition

4.2.1 ***Open System melt-rock reactions***

Orthopyroxene and clinopyroxene, essentially anhydrous minerals in the pyroxene gneisses (Figure 4a), show partial replacement by hydrous minerals hornblende and biotite in all samples examined (Figure 5a, 5b, 5c, 5d). The replacement and hydration reactions are evident from minor partial replacement textures along the grain boundaries of pyroxenes to the full corona texture, where hornblende and quartz symplectite are observed to envelop relict pyroxene grains (Figure 5a; Figure 6a, 6b). Moreover, the replacement texture progresses to a stage where pyroxene grains are inferred to have been completely replaced and pseudomorphed by hornblende and quartz intergrowths (Figure 5b, 5c, 5d).

Apart from the addition of hornblende and biotite to the assemblage as pyroxene gneiss is hydrated, finer and coarser grains of clinozoisite (Figure 4c, Figure 5f, 5g) are found in association with plagioclase in various abundances across the progression of hydration textures. The modal percentage of clinozoisite in the pyroxene gneisses is low, and this increases as the modal proportion of hornblende and biotite increases (Figure 5f, 5g). Furthermore, as the modal proportion of the clinozoisite increases, the modal proportion of pyroxene reduces until pyroxenes are absent. Clinozoisite, a calcium-bearing hydrous mineral, coarsens, progressing from 'dry' pyroxene gneiss to 'wet' hornblende gneiss. Hence, it is inferred that the plagioclase grains in the 'dry' pyroxene gneisses react to form clinozoisite in 'wet' hornblende gneisses (Figure 5e, 5f, 5g). These textural relationships are supported by the mineral mode changes summarized in Table 2.

A final observation in the reaction progression is that the 'dry' pyroxene gneisses have ilmenite as the major accessory oxide mineral (Figure 4a). Ilmenite and titanite are stable under different water activities, so as the rocks become progressively hydrated, ilmenite transitions to form titanite in the 'wet' hornblende gneisses (Figure 6c, 6d).

As inferred from the textural study, anhydrous minerals like diopside and enstatite are replaced by hornblende, a hydrous mineral, and quartz (Figure 5a, 5b, 5c, 5d). Plagioclase with no hydrous component reacts to form a hydrous mineral clinozoisite (Figure 5e, 5f, 5g). The

geochemical plots (Figure 2) show higher SiO_2 in hornblende gneiss compared to pyroxene gneiss in the Western Fiordland Orthogneiss. Hence, it necessitates the presence of a source in an open system, carrying water and silica reacting with the pyroxene gneiss to form hornblende gneiss. The source, in this case, is potentially a hydrous felsic melt, with compositions possibly similar to the Separation Point Suite (Figure 1 & Figure 2, higher SiO_2, K_2O, and lower CaO).

The EBSD maps show that hornblende grains have grown epitaxially along {100} and {010} axis of the pyroxene grains (Figure 9, Figure 10). Minor differences in the {001} axis plots for pyroxene (diopside, enstatite) vs. hornblende are due to the inherent difference in crystallography. The {0001} axis of quartz grains show partial epitaxy with {010} of hornblende and pyroxene (Figure 9). The scatter in quartz data is probably due to the twinning in quartz and recrystallization, possibly during the reaction (Figure 9, Figure 10, Figure 11). This can be observed consistently throughout the rock samples with an increasing modal proportion of hydrous minerals. Also, it can be observed in the 3D crystal models (Figure 13) that the fragments of relict grains of pyroxene show perfect alignment of the crystallographic axis with each other. This indicates that the relict grains of pyroxene once belonged to a single grain that later reacted to form the hornblende and quartz (Figure 13). Hence, it can be inferred that pyroxene minerals are the reactant, with the product minerals hornblende and quartz growing around it.

4.2.2 ***Metasomatism and inferred melt composition***

The geochemical plots show that the 'wet' hornblende gneisses are up to eight times more enriched in Zr compared to the 'dry' pyroxene gneiss, indicating the addition of Zr, which necessitates an open system (Figure 3). The enrichment curve in the hornblende gneisses does not follow the expected trend for an igneous system. Instead, such a high amount of enrichment requires slow and steady episodes of melt fluxes interacting with the rocks spread over a more extended period (Stuart et al., 2018). Moreover, two main pieces of evidence from nano-min mineral mapping (Figure 8): 1) zircons in the 'wet' hornblende gneiss are relatively bigger and higher in number (~20 coarse grains) in comparison to the 'dry' pyroxene gneiss (~3 coarse grains), and 2) dissolution channels, porosity trails, and well-faceted grains indicate the dissolution and reprecipitation of zircon grains, which is possible in the presence of a melt (Halpin et al., 2020). In addition, there is a depletion in the Cr+Ni in the pyroxene gneisses as they transition to the hornblende gneisses (Figure 3).

Further, from the major oxide geochemical data, enrichment of K and Si can be observed in 'wet' hornblende gneiss compared to the 'dry' pyroxene gneiss (Figure 2). Moreover, mainly, depletion of Ca and a minor amount of Mg and Fe can be observed in the 'wet' hornblende gneisses compared to the 'dry' pyroxene gneisses (Figure 2). The geochemical trend indicates that metasomatism was involved as opposed to closed system igneous processes.

All samples contain evidence of the former presence of melt. Even the pyroxene gneiss sample with the least amount of alteration (Figure 4a) has hydrous minerals (< 1%). Felsic minerals like quartz and K-feldspar define microstructures indicative of the former presence of melt (Figure 7, Figure 8) in all the rock samples studied. In addition to crystal orientation analysis, reaction textures with dominantly hydrous and Si-rich minerals as the product (Figure 5a, 5b; Figure 6a, 6b) attest to the presence of melt-rock reaction in an open system. It can be inferred that the melt was probably externally derived, water-bearing, and felsic because it increased the proportion of K, Si, OH, and Zr bearing minerals as the pyroxene gneiss transitioned to the hornblende gneiss. The geochemical patterns linked to the assemblage changes also infer that the melt migrating through the George Sound Shear Zone was enriched in K, Si, and Zr and depleted in Ca, Cr, and Ni compared to the pyroxene gneiss of the rest of the Western Fiordland Orthogneiss.

4.3. Mechanism of melt transfer through the lower and middle arc crust

It can be observed that the grains of plagioclase have undulose extinction and serrated margins in the pyroxene gneiss (Figure 5e, 5f), indicating recrystallization due to deformation in the high strain zones. The grain size of the minerals in the pyroxene gneiss (Figure 4a) initially becomes finer as hydration progresses (Figure 4b). Then the grains coarsen as the proportion of hornblende and quartz increases, and the foliation becomes stronger (Figure 4c). Further, pyroxene grains completely pseudomorphed by hornblende, quartz, and biotite can be observed along with grain size fining and phase mixing (Figure 5b, 5c, 5d). The clusters of the fine-grained hydrous minerals do not show any internal alignment, which is a sign of a low strain (Figure 5c). As opposed to the least hydrated pyroxene gneiss (P77866, Supplementary i), hornblende grains do not show any clusters in the misorientation low angle-axis plot in the hydrated pyroxene gneiss (Supplementary figure ii, iii), indicating no internal deformation of the grains. From these observations, it can be inferred that the solid grains of pyroxene gneiss initially accommodated the deformation in the high strain zone. However, as the hydrous felsic

melt proportion increased in the system, the melt migrating along the mineral grain boundaries accommodated the deformation instead of the solid minerals.

From the dispersed and fine-grained nature of the melt microstructures, it can be inferred that the melt proportion was low, around 8% or less (Dell' Angelo and Tullis, 1988; Walte, Bons, and Passchier, 2005; see also section 1.1.1). Hence in such cases, the buoyant force or interconnectivity of lower melt proportions is not enough to drive melt migration without any external deformation (Maaløe, 1982; Hasalova et al., 2008; Meek et al., 2019).

From all the observations, it can be inferred that the melt flux through the lower crustal Western Fiordland Orthogneiss (WFO) was syn-deformational within the George Sound Shear Zone (GSSZ). As the deformation in the George Sound Shear Zone progressed, it facilitated the melt migration as a conduit. The hydrous, felsic melt reacted with the surrounding 'dry' pyroxene gneisses forming the 'wet' hornblende gneisses.

The gabbroic gneisses in the Western Fiordland Orthogneiss have been studied extensively to understand the field relationships and their formation (Allibone et al., 2009). The differences in geochemistry and petrography in the individual units (e.g., pyroxene gneisses, hornblende gneisses) of the Western Fiordland Orthogneiss were explained in two ways, both of igneous origin (Allibone et al., 2009). One explanation suggested that they were a product of melt from a single source, but the difference in the degree of partial melting of the source rock caused the changes in rock composition (Allibone et al., 2009). Another explanation suggested that different source rocks generated different melt compositions, which crystallized to form the units and hence the difference in chemistry and mineral assemblages, followed by the solid-state deformation due to tectonics (Allibone et al., 2009).

However, this study identified microstructures indicative of the former presence of melt (Figure 7), reaction textures indicating enrichment of K, Si, Zr, and OH in the product minerals (Figures 5, Figure 6, Figure 8), epitaxy in mineral growth (Figure 9, Figure 10, Figure 11), 3D connectivity in the minerals (Figure 12, Figure 13), and dissolution textures in zircon (Figure 8), all of which suggest melt-rock interaction as opposed to an igneous crystallization process. Moreover, the observations have similarities with the microstructure and geochemical trends reported in Meek et al., 2019 and other studies in the nearby Pembroke Valley, indicating melt-rock interaction in high strain zones (Stuart et al., 2016; Stuart et al., 2018; see section 1.1).

The George Sound Shear Zone has an estimated length of ~50 km, a width of ~4 to 10 km (Figure 1) and was active at approximately 30 km deep in the arc. The George Sound Shear Zone exhibits melt flux characteristics and degrees of hydration similar to Style 3 of Stuart et al. (2018), which has an estimated melt flux of 31% to 93%. That is, the volume of melt that migrated through the Style 3 shear zones is approximately one-third to nearly the volume of the deformed and hydrated rock. Therefore, an estimate of the volume of melt that migrated through the George Sound Shear Zone is 62 km^3 to 465 km^3 per kilometre of vertical melt migration. Assuming the melt needs to move from the studied shear zone to volcanoes at the surface (approximately 30 km), maximum estimates of 1,860 km^3 to 13,950 km^3 of melt may have moved through the crust by this mechanism. Hence, this mechanism of melt migration can potentially move a substantial volume of melt up through the crust.

Based on mapped plutonic areas, Milan et al. (2017) determined that magma addition rates in the Fiordland arc increased at approximately 130 million years ago, from ~14 km^3/my per km of arc to ~100 km^3/my per km of arc. The George Sound Shear Zone was possibly active for a maximum of 8 million years (Marcotte et al., 2005) over its 50km arc length, and as such, may have accommodated 5,600–40,000 km^3 of magma added to the arc. As these values exceed those calculated above, melt migration through the George Sound Shear Zone was likely active for about a million years or less.

If each piece of evidence discussed above is observed individually, it might indicate a classic igneous origin for the hornblende gneisses in and around George Sound Shear Zone in the Western Fiordland Orthogneiss. However, all the evidence, when combined, indicates a metamorphic origin. See Table 3 for a comparison of igneous versus melt-rock interaction interpretations. In the map view, the shape of the region rich in hornblende gneisses does not resemble a pluton, as it is an elongate patch along the George Sound Shear Zone (marked in green, Figure 1). One might argue that the hornblende gneiss is formed from a kilometer-long dyke, but it does not have sharp contacts or chilled margins. Rather, the rocks adjacent to the hornblende gneiss transition from hydrated pyroxene gneiss to pyroxene gneiss as one moves farther away from the George Sound Shear Zone (Figure 1). There is the co-occurrence of reaction textures (Figure 5, Figure 6), microstructures indicative of the former melt presence (Figure 7), zircon reprecipitation, and dissolution textures (Figure 8) in the same thin sections, along with the enrichment and depletion of elements. This is observed in the rocks along the kilometer-wide stretches of the George Sound Shear Zone in Worsley Pluton, Misty Pluton, and

Mckerr Intrusives (Figure 1). Hence, it can be argued that such observations necessitate the presence of an external melt reacting with the surrounding pyroxene gneiss to produce hornblende gneiss, where the reaction was stronger in the vicinity of the George Sound Shear Zone as compared to the rocks farther away (Figure 14).

Hence, it can be interpreted that the Western Fiordland Orthogneiss was initially a pyroxene gneiss dominantly composed of clinopyroxene, orthopyroxene, and plagioclase (Figure 14, stage 1). The George Sound Shear Zone (GSSZ), cutting across the lower crustal magmatic arc and the Western Fiordland Orthogneiss, facilitated the diffuse melt transfer from the mantle below (Figure 14, stage 2). The melt transfer was syn-deformational, with diffuse porous flow along the grain boundary of the minerals in the host rock (i.e., pyroxene gneiss). During migration, the melt reacted with the surrounding pyroxene gneiss, hydrating the rock and enriching it with felsic and hydrous minerals. This, over time, formed the hornblende bearing gneisses along the kilometer-long and wide George Sound Shear Zone in the Western Fiordland Orthogneiss (Figure 1).

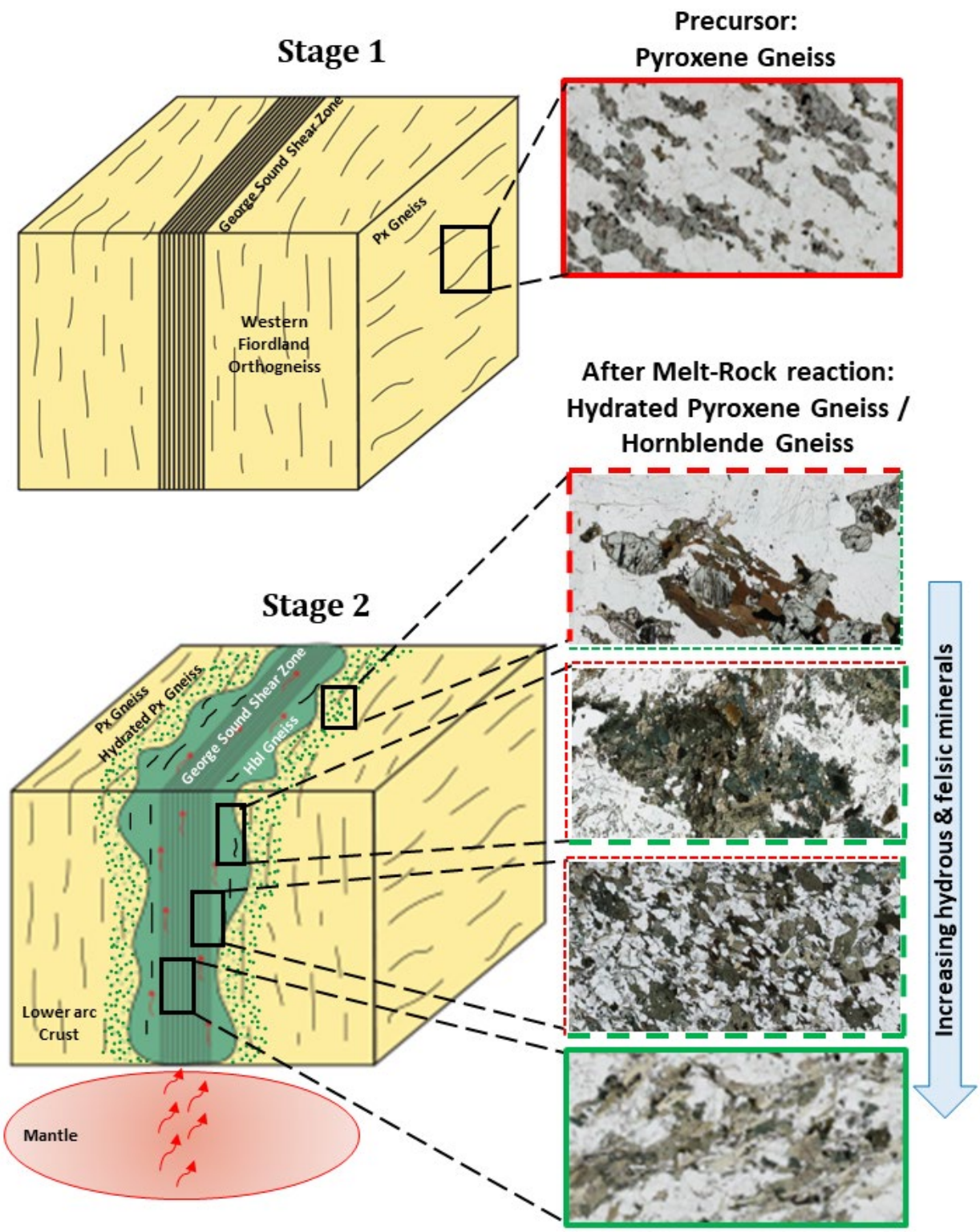

Figure 14: *Schematic model showing the two-stage evolution (119-111 Ma; Marcotte et al., 2005) of the hornblende gneiss in the Western Fiordland Orthogneiss (128-114 Ma; Schwartz et al., 2017) via deformation-assisted diffuse porous melt transfer through the George Sound Shear Zone (~50 km in length and ~4–10 km in width). On the right panel, the progression of the melt-rock reaction is shown by the photomicrographs (pyroxene gneiss in* ***red*** *outline, hydrated pyroxene gneiss in* ***red & green dashed*** *outline of varying thickness showing the progression of hydration reaction, hornblende gneiss in* ***green*** *outline).*

***Table 3**: Comparison between a classic igneous origin vs. melt-rock interaction interpretation of Hornblende gneisses of the Western Fiordland Orthogneiss.*

Parameter	Igneous Process	Melt-Rock Interaction
Formation	Primary hydrous magma	Two-step approach - protolith of pyroxene gneiss - melt rock interaction with the hydrous melt - moving through GSSZ
Field scale	Field scale – more homogenous rock across a larger area	Heterogeneous rock depends on melt migration pathways, for example, heterogeneity in grain size, mineral assemblage
Strain	Low strain in the minerals, as it is liquid supported	Some strain in the rock, in the form of strong foliation, CPO, minor undulose extinction
Reaction Textures	Low abundance of reaction textures	High abundance of reaction textures; i) enstatite, diopside to hornblende ii) plagioclase to clinozoisite iii)ilmenite to titanite
Grain shape	Subhedral grains	Polygonal grains, serrated boundary, and crystal faces form where they are adjacent to pockets of melt
Twinning/ Zoning	Growth twining or oscillatory zoning in plagioclase	Deformation twinning in non-melt grains (i.e., the solid component of the melt-rock system)
Geochemistry	"Classic" geochemical trends in an igneous suite.	Unusual whole rock compositions formed by metasomatism (section 1.1.3, Meek et al.,2019)

Chapter 5: CONCLUSION

Lower crustal migration of melt is crucial in determining crustal rheology, besides its fundamental control on the chemical evolution of the Earth's crust. Crustal scale melt migration pathways facilitate mass and heat transfer. This results in the potential enrichment of minerals and a high geothermal gradient. Hence, understanding the thermal and chemical dynamics of the lower arc crust is vital for discovering new ore deposits and tapping geothermal energy, two crucial resources for society. Thus, understanding the melt transfer processes, especially in the lower crust, is essential.

This project focuses on the well-preserved plutonic lower crustal arc rocks of the Western Fiordland Orthogneiss, Fiordland, New Zealand. As opposed to a classic igneous origin, it provides an alternative hypothesis for the formation of hornblende gneiss in the Western Fiordland Orthogneiss. It further provides an understanding of melt transfer from the mantle to the lower arc crust, which is important in understanding the evolution of the Earth through time. The detailed geochemical and microstructural study brings out the mineral scale reaction mechanisms. Microstructural evidence is used to argue for the former presence of melt in all rocks studied. An open system of melt flux is inferred from evidence of reactions and changes to whole rock geochemical patterns. Deformation-assisted diffuse porous melt flow is interpreted as the key mechanism of melt migration. This study uniquely identifies the importance of the syn-deformational diffuse porous melt flow mechanism in the evolution of the hornblende gneisses in and around the George Sound Shear Zone in specific and lower crustal arcs in general.

Some of the future works that would enrich our current understanding of the Western Fiordland Orthogneiss and lower crustal arcs are as follows: 1) re-assessing the geological map of Fiordland, New Zealand by conducting fieldwork and studying well-constrained samples, with the focus to investigate the scale of mass transport and volume of melt flux, 2) detailed elemental mapping of the minerals to study the melt pathways, 3) experiments to better understand the melt transfer, associated microstructure formation process, and step-wise study of the geochemical changes, 4) Pb-U dating in zircon to constrain the age of the units and duration of the processes, and 5) application of the knowledge and the indicators established in the current project to study other lower crustal arcs that are not as well-preserved.

Supplementary Data

The link below contains the whole-rock geochemical data set:

WFO_SPS_MResDataSheet.xlsx

REFERENCES

Allibone, A. H., Milan, L. A., Daczko, N. R., & Turnbull, I. M. (2009). Granulite facies thermal aureoles and metastable amphibolite facies assemblages adjacent to the Western Fiordland Orthogneiss in southwest Fiordland, New Zealand. *Journal of Metamorphic Geology*, *27*(5), 349-369.

Allibone, A. H., Jongens, R., Turnbull, I. M., Milan, L. A., Daczko, N. R., DePaoli, M. C., & Tulloch, A. J. (2009). Plutonic rocks of Western Fiordland, New Zealand: Field relations, geochemistry, correlation, and nomenclature. *New Zealand Journal of Geology and Geophysics*, *52*(4), 379-415.

Allibone, A. H., Jongens, R., Scott, J. M., Tulloch, A. J., Turnbull, I. M., Cooper, A. F., Powell, N.G., Ladley, E.B., King, R.P., & Rattenbury, M. S. (2009). Plutonic rocks of the Median Batholith in eastern and central Fiordland, New Zealand: Field relations, geochemistry, correlation, and nomenclature. *New Zealand Journal of Geology and Geophysics*, *52*(2), 101-148.

Anderson, I., Stowell, H. H., Schwartz, J. J., Klepeis, K. A., Bollen, E. M., & Miranda, E. A. (2019, January). Pressure, Temperature, and Timing of Magma Intrusion and Metamorphism, George Sound New Zealand. In *Geological Society of America Abstracts with Programs*.

Bradshaw, J. Y. (1989). Early Cretaceous vein-related garnet granulite in Fiordland, southwest New Zealand: a case for infiltration of mantle-derived CO_2-rich fluids. *The Journal of Geology*, *97*(6), 697-717.

Bradshaw, J. Y. (1990). Geology of crystalline rocks of northern Fiordland: details of the granulite facies Western Fiordland Orthogneiss and associated rock units. *New Zealand journal of geology and geophysics*, *33*(3), 465-484.

Bradshaw, J. Y., & Kimbrough, D. L. (1991). Mid-Paleozoic age of granitoids in enclaves within Early Cretaceous granulites, Fiordland, southwest New Zealand. *New Zealand journal of geology and geophysics*, *34*(4), 455-469.

Beach, A., & Fyfe, W. S. (1972). Fluid transport and shear zones at Scourie, Sutherland: evidence of overthrusting? *Contributions to Mineralogy and Petrology*, *36*(3), 175-180.

Beere, W. (1975). A unifying theory of the stability of penetrating liquid phases and sintering pores. *Acta Metallurgica*, *23*(1), 131-138.

Breton, N. L., & Thompson, A. B. (1988). Fluid-absent (dehydration) melting of biotite in metapelites in the early stages of crustal anatexis. *Contributions to Mineralogy and Petrology*, *99*(2), 226-237.

Brown, M. (2004). The mechanism of melt extraction from lower continental crust of orogens. *Earth and Environmental Science Transactions of the Royal Society of Edinburgh*, *95*(1-2), 35-48.

Brown, M. (2010). Melting of the continental crust during orogenesis: the thermal, rheological, and compositional consequences of melt transport from lower to upper continental crust. *Canadian Journal of Earth Sciences*, *47*(5), 655-694.

Brown, M., & Solar, G. S. (1998). Shear-zone systems and melts: feedback relations and self-organization in orogenic belts. *Journal of structural geology*, *20*(2-3), 211-227.

Carter, K. E., & Dworkin, S. I. (1990). Channelized fluid flow through shear zones during fluid-enhanced dynamic recrystallization, Northern Apennines, Italy. *Geology*, *18*(8), 720-723.

Cartwright, I., & Barnicoat, A. C. (2003). Geochemical and stable isotope resetting in shear zones from Täschalp: constraints on fluid flow during exhumation in the Western Alps. *Journal of Metamorphic Geology*, *21*(2), 143-161.

Collins, W. J., & Sawyer, E. W. (1996). Pervasive granitoid magma transfer through the lower–middle crust during non-coaxial compressional deformation. *Journal of Metamorphic Geology*, *14*(5), 565-579.

Clark, A. R. C. (2017). Slab-triggered arc flare-up in the Cretaceous Median Batholith and the growth of lower arc crust, Fiordland, New Zealand. *Journal of Petrology*, *58*(6), 1145-1171.

Corfu, F., Hanchar, J. M., Hoskin, P. W., & Kinny, P. (2003). Atlas of zircon textures. *Reviews in mineralogy and geochemistry*, *53*(1), 469-500.

Decker, M., Schwartz, J. J., Stowell, H. H., Klepeis, K. A., Tulloch, A. J., Kitajima, K., Valley, J. W., & Kylander-Clark, A. R. C. (2017). Slab-triggered arc flare-up in the Cretaceous Median Batholith and the growth of lower arc crust, Fiordland, New Zealand. *Journal of Petrology*, *58*(6), 1145-1171.

Degeling, H.S. (1997). Mid-crustal Response to Syn-Tectonic Pluton Emplacement. Unpublished BSc (Hons) thesis, University of Sydney, Sydney.

Dell'Angelo, L. N., & Tullis, J. (1988). Experimental deformation of partially melted granitic aggregates. *Journal of metamorphic Geology*, *6*(4), 495-515.

Daczko, N. R., Piazolo, S., Meek, U., Stuart, C. A., & Elliott, V. (2016). Hornblendite delineates zones of mass transfer through the lower crust. *Scientific Reports*, *6*(1), 1-6.

Etheridge, M. A., Daczko, N. R., Chapman, T., & Stuart, C. A. (2021). Mechanisms of melt extraction during lower crustal partial melting. *Journal of Metamorphic Geology*, *39*(1), 57-75.

Halpin, J. A., Daczko, N. R., Direen, N. G., Mulder, J. A., Murphy, R. C., & Ishihara, T. (2020). Provenance of rifted continental crust at the nexus of East Gondwana breakup. *Lithos*, *354*, 105363.

Harte, B., Pattison, D. R. M., & Linklater, C. M. (1991). Field relations and petrography of partially melted pelitic and semi-pelitic rocks. In *Equilibrium and kinetics in contact metamorphism* (pp. 181-209). Springer, Berlin, Heidelberg.

Hasalova, P., Schulmann, K., Lexa, O., Štípská, P., Hrouda, F., Ulrich, S., Haloda, J., & Týcová, P. (2008). Origin of migmatites by deformation-enhanced melt infiltration of orthogneiss: A new model based on quantitative microstructural analysis. *Journal of Metamorphic Geology*, *26*(1), 29-53.

Holness, M. B. (2006). Melt–solid dihedral angles of common minerals in natural rocks. *Journal of Petrology*, *47*(4), 791-800.

Holness, M. B., & Sawyer, E. W. (2008). On the pseudomorphing of melt-filled pores during the crystallization of migmatites. *Journal of Petrology*, *49*(7), 1343-1363.

Holness, M. B., & Clemens, J. D. (1999). Partial melting of the Appin Quartzite driven by fracture-controlled H2O infiltration in the aureole of the Ballachulish Igneous Complex, Scottish Highlands. *Contributions to Mineralogy and Petrology*, *136*(1), 154-168.

Holyoke III, C. W., & Tullis, J. (2006). The interaction between reaction and deformation: an experimental study using a biotite+ plagioclase+ quartz gneiss. *Journal of Metamorphic Geology*, *24*(8), 743-762.

Holyoke III, C. W., & Tullis, J. (2006). Mechanisms of weak phase interconnection and the effects of phase strength contrast on fabric development. *Journal of Structural Geology*, *28*(4), 621-640.

Klepeis, K. A., Clarke, G. L., Gehrels, G., & Vervoort, J. (2004). Processes controlling vertical coupling and decoupling between the upper and lower crust of orogens: Results from Fiordland, New Zealand. *Journal of Structural Geology*, *26*(4), 765-791.

Klepeis, K., & Webb, L. (2019). Deep slab collision during Miocene subduction causes uplift along crustal-scale reverse faults in Fiordland, New Zealand. *GSA today*.

Laporte, D. (1994). Wetting behavior of partial melts during crustal anatexis: the distribution of hydrous silicic melts in polycrystalline aggregates of quartz. *Contributions to Mineralogy and Petrology*, *116*(4), 486-499.

Levine, J. S., Mosher, S., & Siddoway, C. S. (2013). Relationship between syndeformational partial melting and crustal-scale magmatism and tectonism across the Wet Mountains, central Colorado. *Lithosphere*, *5*(5), 456-476.

Lindquist, P. C. (2020). *The architecture of a lower-crustal shear zone and evidence for along-strike variations in strain localization and partitioning, Fiordland, New Zealand*. Master thesis, The University of Vermont and State Agricultural College.

Maaløe, S. (1982). Geochemical aspects of permeability controlled partial melting and fractional crystallization. *Geochimica et Cosmochimica Acta*, *46*(1), 43-57.

Marchildon, N., & Brown, M. (2002). Grain-scale melt distribution in two contact aureole rocks: Implications for controls on melt localization and deformation. *Journal of Metamorphic Geology*, *20*(4), 381-396.

Meek, U., Piazolo, S., & Daczko, N. R. (2019). The field and microstructural signatures of deformation-assisted melt transfer: Insights from magmatic arc lower crust, New Zealand. *Journal of Metamorphic Geology*, *37*(6), 795-821.

Mezger, K., & Krogstad, E. J. (1997). Interpretation of discordant U-Pb zircon ages: An evaluation. *Journal of metamorphic Geology*, *15*(1), 127-140.

Mortimer, N., Tulloch, A. J., Spark, R. N., Walker, N. W., Ladley, E., Allibone, A., & Kimbrough, D. L. (1999). Overview of the Median Batholith, New Zealand: a new interpretation of the geology of the Median Tectonic Zone and adjacent rocks. *Journal of African earth sciences*, *29*(1), 257-268.

Morisset, C. E., & Scoates, J. S. (2008). Origin of zircon rims around ilmenite in mafic plutonic rocks of Proterozoic anorthosite suites. *The Canadian Mineralogist*, *46*(2), 289-304.

Pidgeon, R. T., Nemchin, A. A., & Hitchen, G. J. (1998). Internal structures of zircons from Archaean granites from the Darling Range batholith: implications for zircon stability and the interpretation of zircon U-Pb ages. *Contributions to Mineralogy and Petrology*, *132*(3), 288-299.

Prior, D. J., Trimby, P. W., Weber, U. D., & Dingley, D. J. (1996). Orientation contrast imaging of microstructures in rocks using forescatter detectors in the scanning electron microscope. *Mineralogical Magazine*, *60*(403), 859-869.

Prior, D. J., Wheeler, J., Peruzzo, L., Spiess, R., & Storey, C. (2002). Some garnet microstructures: an illustration of the potential of orientation maps and misorientation analysis in microstructural studies. *Journal of Structural Geology*, *24*(6-7), 999-1011.

Roberts, M. P., & Finger, F. (1997). Do U-Pb zircon ages from granulites reflect peak metamorphic conditions?. *Geology*, *25*(4), 319-322.

Rosenberg, C. L., & Riller, U. (2000). Partial-melt topology in statically and dynamically recrystallized granite. *Geology*, *28*(1), 7-10.

Rosenberg, C. L., & Handy, M. R. (2005). Experimental deformation of partially melted granite revisited: implications for the continental crust. *Journal of metamorphic Geology*, *23*(1), 19-28.

Robin, P.Y. F. (1979). Theory of metamorphic segregation and related processes. *Geochimica et Cosmochimica Acta*, *43*, 1587–1600.

Rudnick, R. L. (1995). Making continental crust. *Nature*, *378*(6557), 571-578.

Sawyer, E. W. (1994). Melt segregation in the continental crust. *Geology*, *22*(11), 1019-1022.

Sawyer, E. W. (1999). Criteria for the recognition of partial melting. *Physics and Chemistry of the Earth, Part A: Solid Earth and Geodesy*, *24*(3), 269-279.

Sawyer, E. W. (2001). Melt segregation in the continental crust: distribution and movement of melt in anatectic rocks. *Journal of metamorphic Geology*, *19*(3), 291-309.

Schaltegger, U., Fanning, C. M., Günther, D., Maurin, J. C., Schulmann, K., & Gebauer, D. (1999). Growth, annealing and recrystallization of zircon and preservation of monazite in high-grade metamorphism: conventional and in-situ U-Pb isotope, cathodoluminescence and microchemical evidence. *Contributions to Mineralogy and Petrology*, *134*(2), 186-201.

Schwartz, J. J., Klepeis, K. A., Sadorski, J. F., Stowell, H. H., Tulloch, A. J., & Coble, M. A. (2017). The tempo of continental arc construction in the Mesozoic Median Batholith, Fiordland, New Zealand. *Lithosphere*, *9*(3), 343-365.

Sleep, N. H. (1988). Tapping of melt by veins and dikes. *Journal of Geophysical Research: Solid Earth*, *93*(B9), 10255-10272.

Spence, D. A., Sharp, P. W., & Turcotte, D. L. (1987). Buoyancy-driven crack propagation: a mechanism for magma migration. *Journal of Fluid Mechanics*, *174*, 135-153.

Stuart, C. A., Daczko, N. R., & Piazolo, S. (2017). Local partial melting of the lower crust triggered by hydration through melt–rock interaction: an example from Fiordland, New Zealand. *Journal of Metamorphic Geology*, *35*(2), 213-230.

Stuart, C. A., Piazolo, S., & Daczko, N. R. (2016). Mass transfer in the lower crust: Evidence for incipient melt assisted flow along grain boundaries in the deep arc granulites of Fiordland, New Zealand. *Geochemistry, Geophysics, Geosystems*, *17*(9), 3733-3753.

Stuart, C. A., Meek, U., Daczko, N. R., Piazolo, S., & Huang, J. X. (2018). Chemical signatures of melt–rock interaction in the root of a magmatic arc. *Journal of Petrology*, *59*(2), 321-340.

Stuart, C. A., Piazolo, S., & Daczko, N. R. (2018). The recognition of former melt flux through high-strain zones. *Journal of Metamorphic Geology*, *36*(8), 1049-1069.

Tulloch, A. J., Ireland, T. R., Kimbrough, D. L., Griffin, W. L., & Ramezani, J. (2011). Autochthonous inheritance of zircon through Cretaceous partial melting of Carboniferous plutons: the Arthur River Complex, Fiordland, New Zealand. *Contributions to Mineralogy and Petrology*, *161*(3), 401-421.

Tulloch, A. J., & Kimbrough, D. L. (2003). Paired plutonic belts in convergent margins and the development of high Sr/Y magmatism: Peninsular Ranges Batholith of Baja California and Median Batholith of New Zealand.

Vanderhaeghe, O. (1999). Pervasive melt migration from migmatites to leucogranite in the Shuswap metamorphic core complex, Canada: control of regional deformation. *Tectonophysics*, *312*(1), 35-55.

Van der Molen, I., & Paterson, M. S. (1979). Experimental deformation of partially-melted granite. *Contributions to Mineralogy and Petrology*, *70*(3), 299-318.

Vavra, G., Schmid, R., & Gebauer, D. (1999). Internal morphology, habit and U-Th-Pb microanalysis of amphibolite-to-granulite facies zircons: geochronology of the Ivrea Zone (Southern Alps). *Contributions to Mineralogy and Petrology*, *134*(4), 380-404.

Vernon, R. H. (2011). Microstructures of melt-bearing regional metamorphic rocks. *Geological Society of America Memoirs*, *207*, 1-11.

Walte, N. P., Bons, P. D., & Passchier, C. W. (2005). Deformation of melt-bearing systems - insight from in situ grain-scale analogue experiments. *Journal of Structural Geology*, *27*(9), 1666-1679.

Whitney, D. L., & Evans, B. W. (2010). Abbreviations for names of rock-forming minerals. *American Mineralogist*, *95*(1), 185-187.

Weinberg, R. F. (1996). Ascent mechanism of felsic magmas: news and views. *Earth and Environmental Science Transactions of the Royal Society of Edinburgh*, *87*(1-2), 95-103.

Winter, J. D. (2014). Principles of Igneous and Metamorphic Petrology John D. *Winter, Harlow Pearson Education*.

Zheng, Y. F. (2019). Subduction zone geochemistry. *Geoscience Frontiers*, *10*(4), 1223-1254.

Appendix

This section contains additional figures from the Electron backscatter diffraction (EBSD) analysis. They include pole figures for crystal preferred orientation (CPO; discussed in section 3.4) and enlarged versions of the epitaxial growth of minerals (Discussed in Figures 9, 10, 11).

P77866

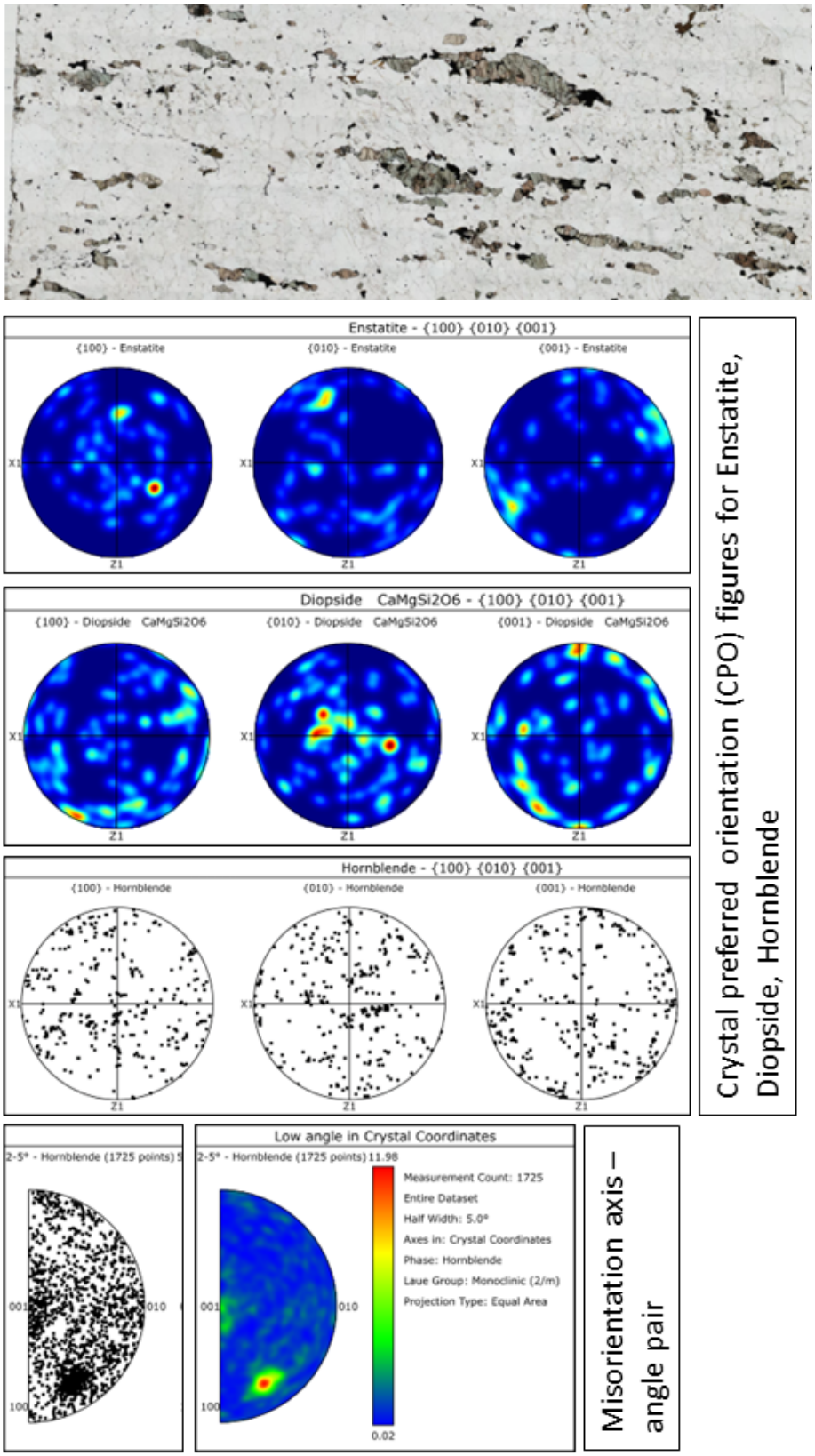

Supplementary Figure (i)*: EBSD analysis for pyroxene gneiss P77866 showing: 1) CPO (one point per crystallite) pole figures with a weak orientation for the minerals, especially hornblende, and 2) misorientation axis-angle pair showing low angle axis cluster formation in hornblende. NOTE: CPO plots are in the XZ section.*

9704 (i)

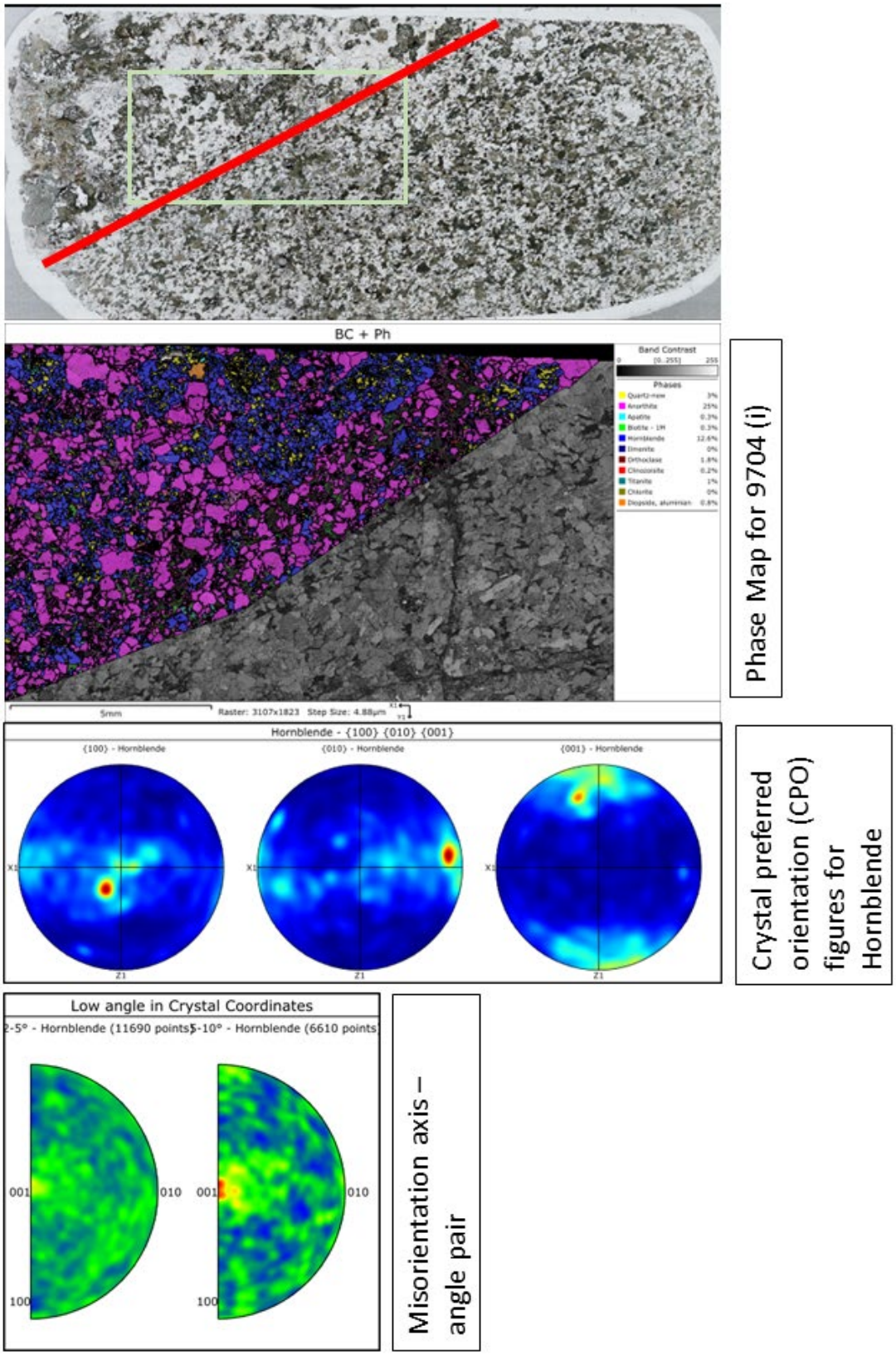

Supplementary Figure (ii)*: EBSD analysis for the coarse grained part of partially hydrated pyroxene gneiss, 9704 (i) showing: 1) CPO (one point per crystallite) pole figures with a stronger orientation for hornblende as compared to P77866, and 2) misorientation axis-angle pair showing no strong low angle axis cluster for hornblende. NOTE: CPO plots are in the XZ section.*

9704 (ii)

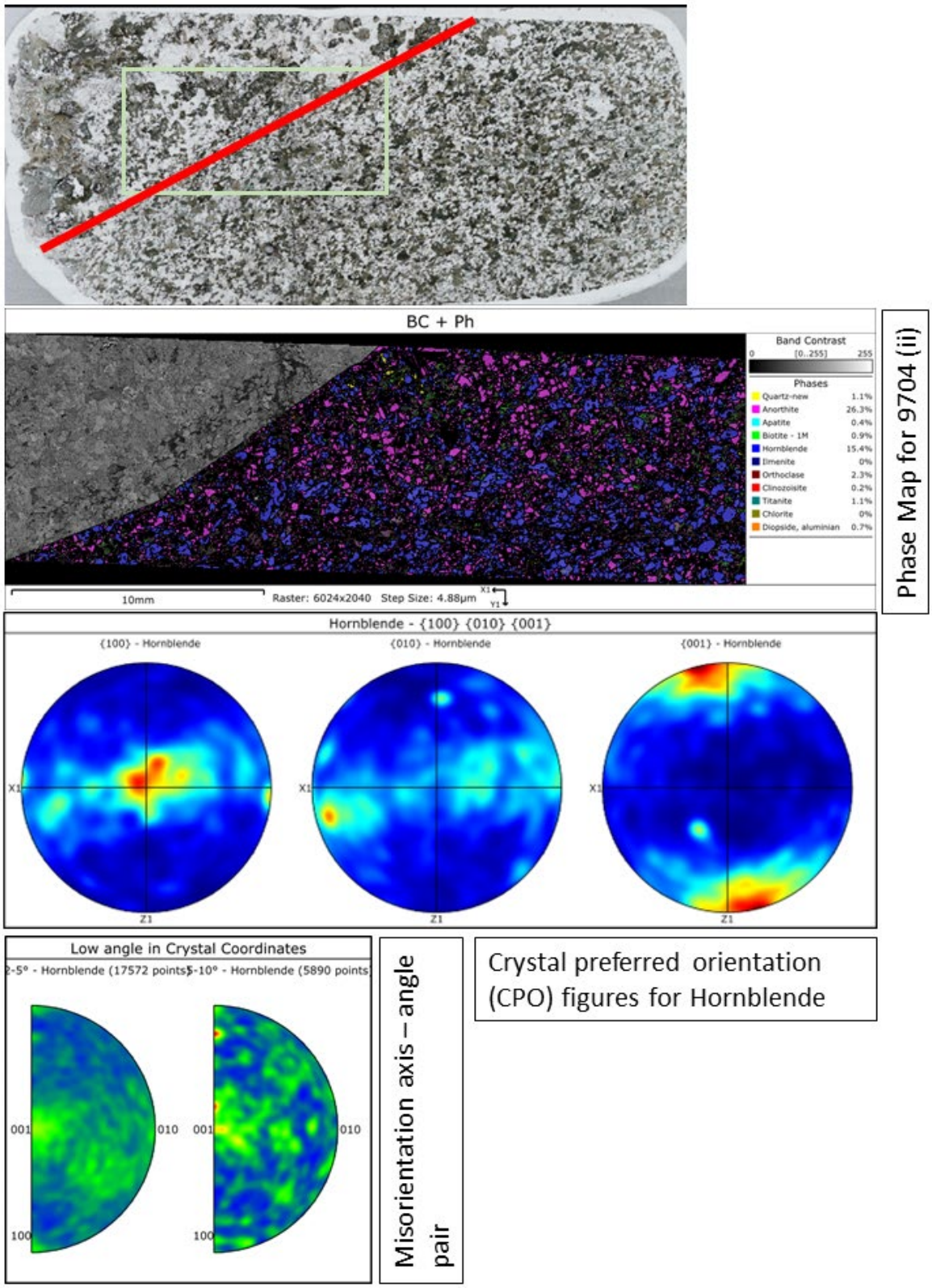

Supplementary Figure (iii)*: EBSD analysis for the fine-grained part of partially hydrated pyroxene gneiss, 9704 (ii) showing: 1) CPO (one point per crystallite) pole figures with a stronger orientation for hornblende as compared to 9704 (i), and 2) misorientation axis-angle pair showing no strong low angle cluster for hornblende. NOTE: CPO plots are in the XZ section.*

9704

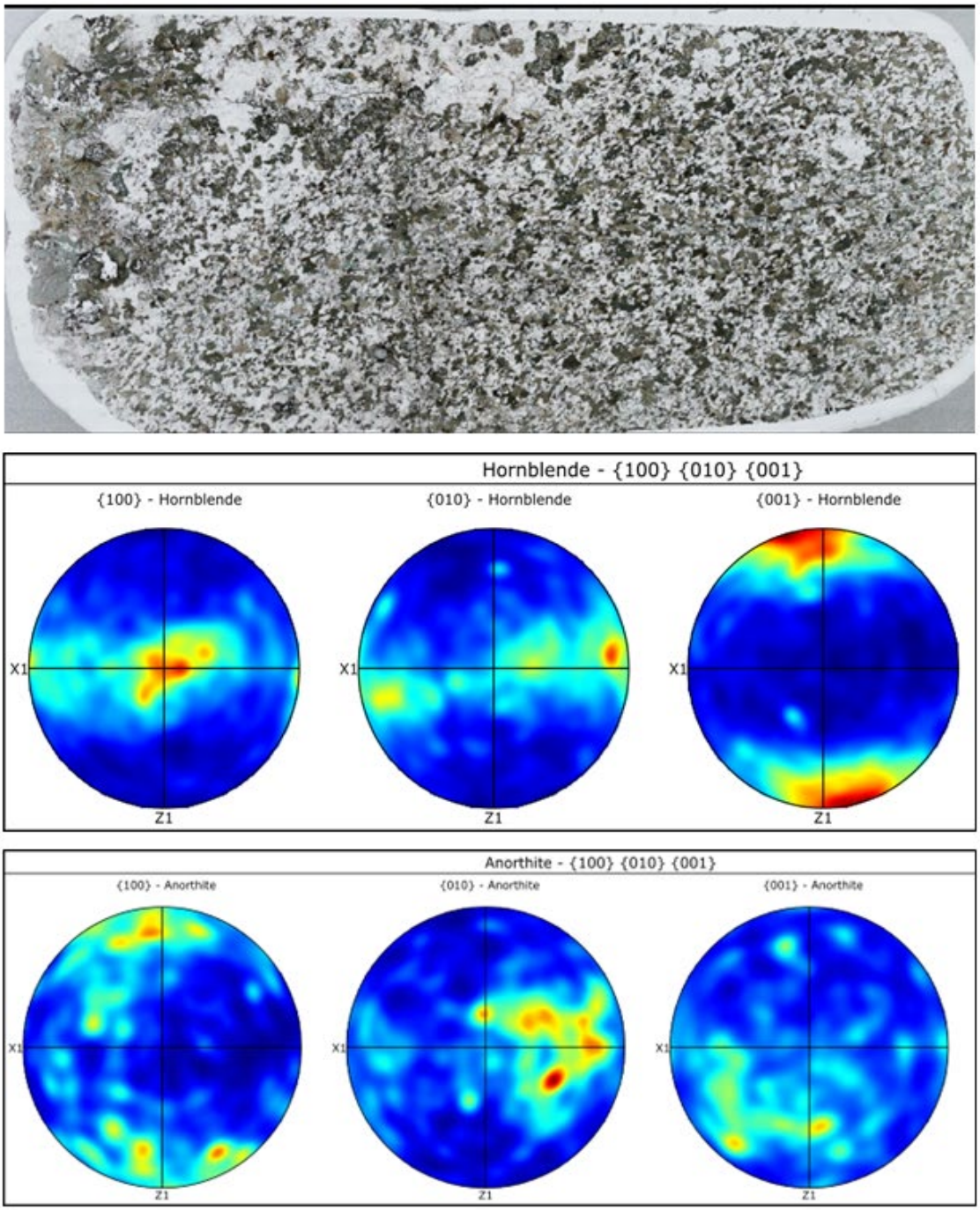

Crystal preferred orientation (CPO) figures for Hornblende and Anorthite

Supplementary Figure (iv)*: EBSD analysis for the whole thin section of the partially hydrated pyroxene gneiss, 9704 showing: 1) CPO (one point per crystallite) pole figures with a strong orientation for hornblende as compared to P77866. NOTE: CPO plots are in the XZ section.*

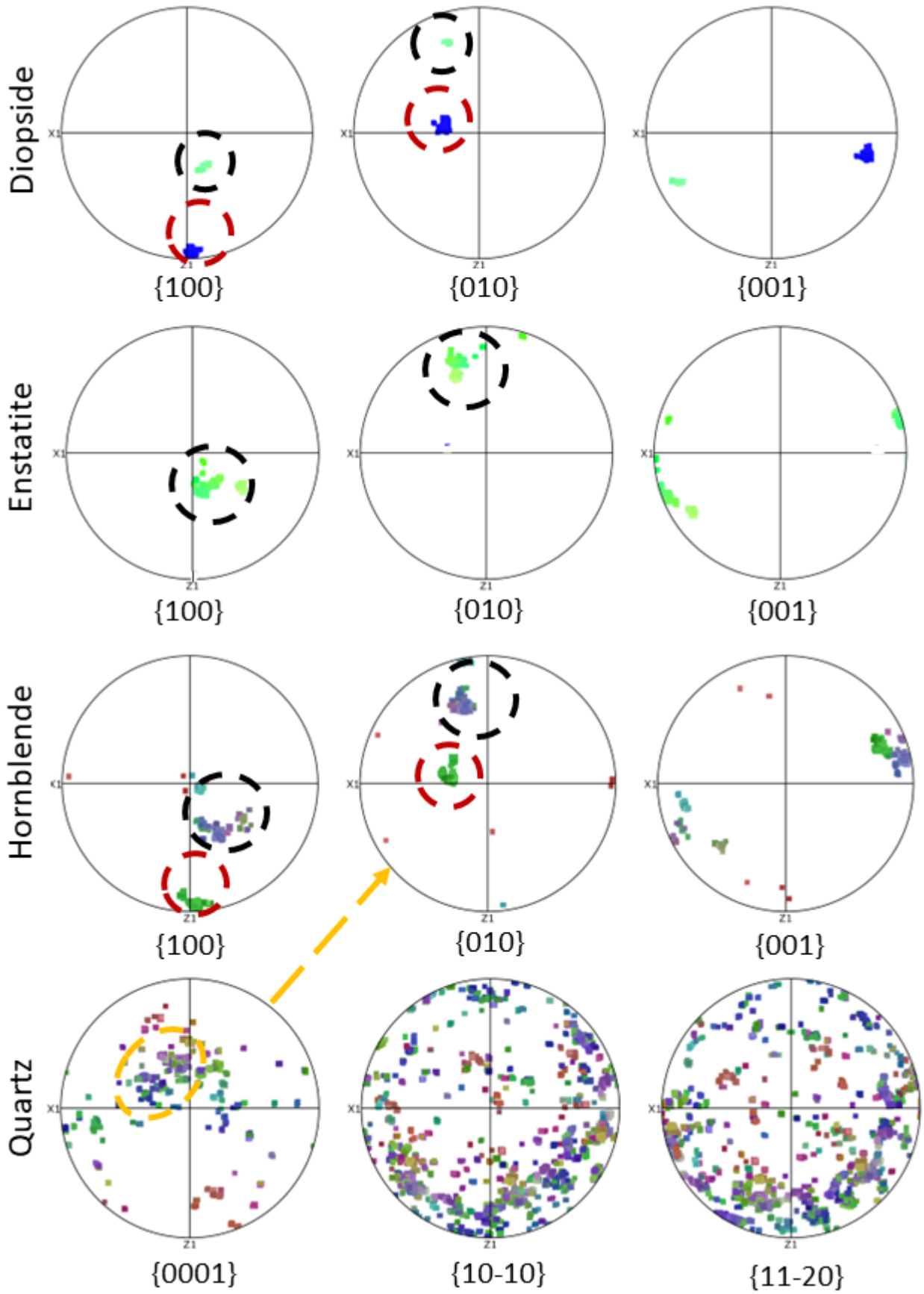

***Supplementary Figure (v)**: Enlarged version of the XZ pole figures showing the epitaxial orientation of minerals (dashed circle) as discussed in Figure 9 in this thesis.*

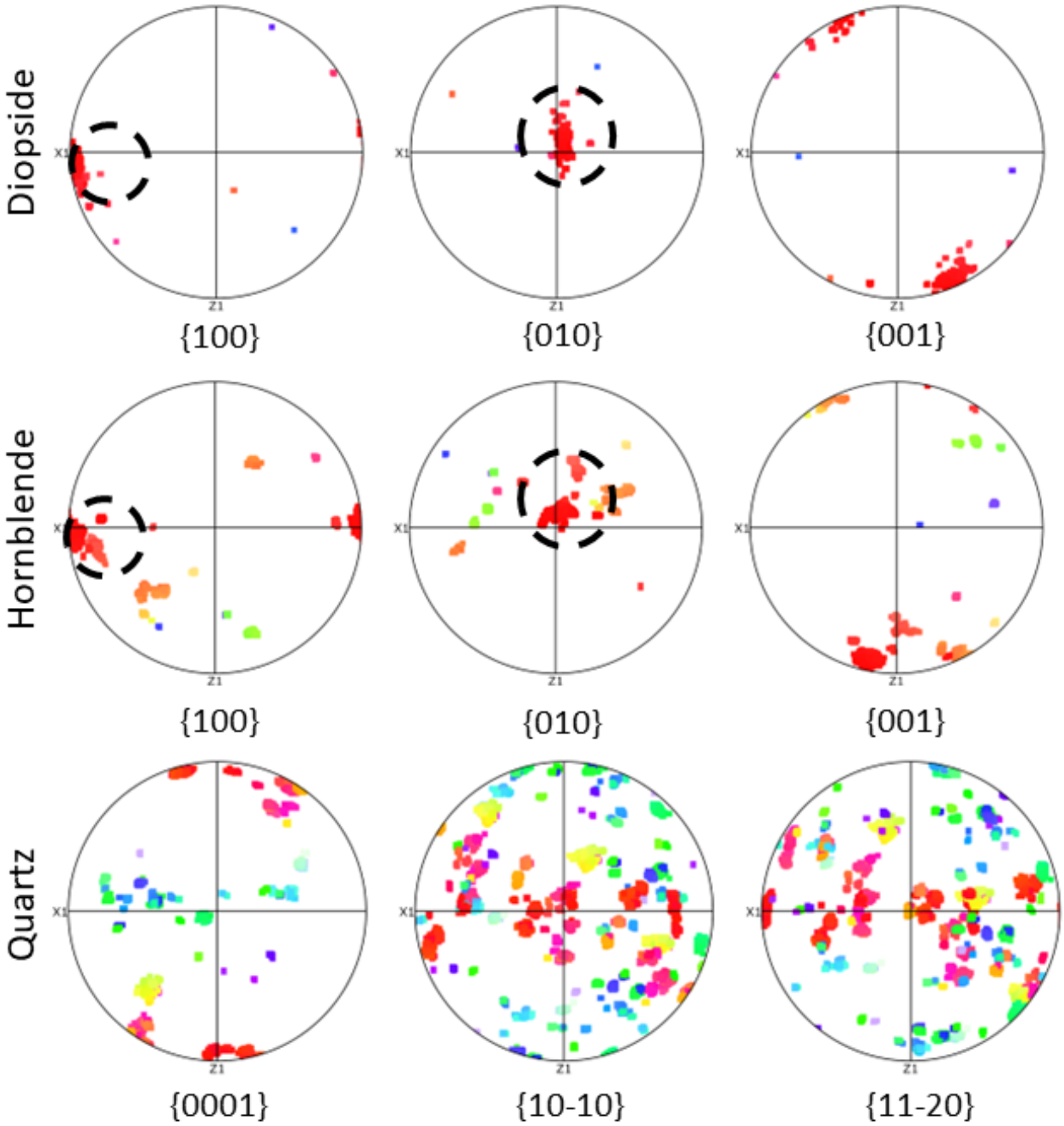

Supplementary Figure (vi)*: Enlarged version of the XZ pole figures showing the epitaxial orientation of minerals (dashed circles) as discussed in Figure 10 in this thesis.*

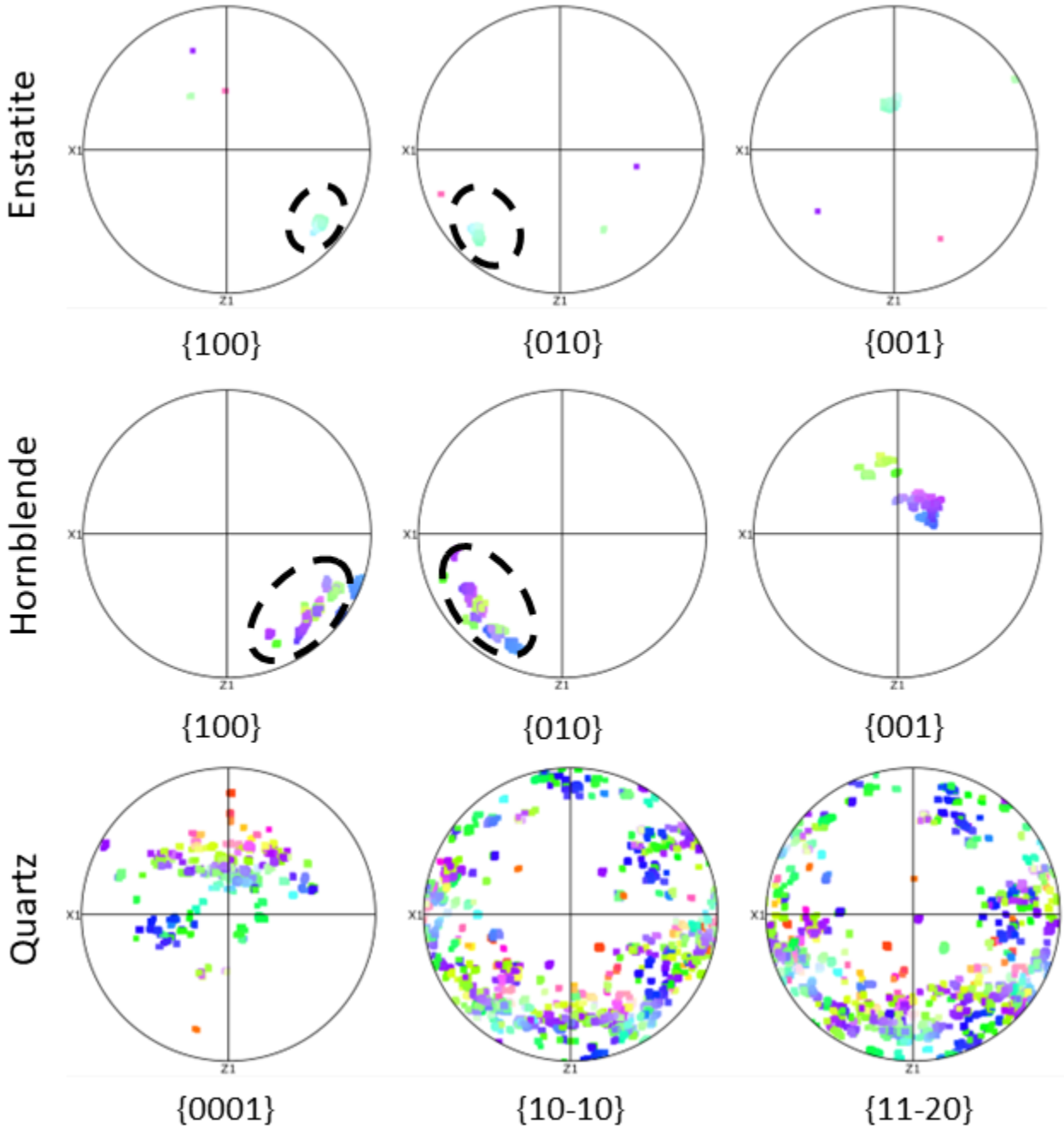

Supplementary Figure (vii)*: Enlarged version of the XZ pole figures showing the epitaxial orientation of minerals (dashed circles) as discussed in Figure 11 in this thesis.*